Pyry Kivisaari

# The Effect of Current Injection Geometry on Current Spreading in Semiconductor LEDs

**Faculty of Information and Natural Sciences**

Thesis submitted for examination for the degree of Master of Science in Technology.

Espoo 4.10.2010

**Thesis supervisor:**

Prof. Jukka Tulkki

**Thesis instructor:**

Dr.Tech. Jani Oksanen

Aalto University
School of Science
and Technology

AALTO UNIVERSITY
SCHOOL OF SCIENCE AND TECHNOLOGY

ABSTRACT OF THE
MASTER'S THESIS

Author: Pyry Kivisaari

Title: The Effect of Current Injection Geometry on Current Spreading in Semiconductor LEDs

Date: 4.10.2010 Language: English Number of pages: 8+62

Faculty of Information and Natural Sciences

Department of Biomedical Engineering and Computational Science

Professorship: Computational Science Code: S-114

Supervisor: Prof. Jukka Tulkki

Instructor: Dr.Tech. Jani Oksanen

In this thesis the physical models needed in simulating the operation of semiconductor LEDs are reviewed and used to numerically model the operation of two different LED structures. The numerical models are solved with the finite element method and the simulated structures are variations of the thin-film flip-chip and transverse multi-quantum well LEDs which are recently proposed structures for efficient white light generation.

The numerical models used in this thesis are based on Maxwell's equations, Fermi-Dirac statistics, semiconductor current equations and basic recombination models. Modeled materials are nitride semiconductors which exhibit strong spontaneous and piezoelectric polarization fields, and these fields are also included in the models.

The two above mentioned LED structures are compared with each other in terms of the current injection properties, overall efficiency, light output power and the frequency distribution of the generated light. The effect of the current injection layer width on the efficiency is studied as well. In addition, the effect of the spontaneous and piezoelectric polarization fields on the LED operation and efficiency is investigated.

Keywords: Solid state lighting, Light-emitting diodes, Nitride semiconductors, Thin-film flip-chip LEDs, Transverse multi-quantum well LEDs, Efficiency, Numerical modeling, FEM

AALTO-YLIOPISTO
TEKNILLINEN KORKEAKOULU

DIPLOMITYÖN
TIIVISTELMÄ

Tekijä: Pyry Kivisaari

Työn nimi: Injektiogeometrian vaikutus sähkövirran jakautumiseen puolijohdeledeissä

Päivämäärä: 4.10.2010 Kieli: Englanti Sivumäärä: 8+62

Informaatio- ja luonnontieteiden tiedekunta

Lääketieteellisen tekniikan ja laskennallisen tieteen laitos

Professuuri: Laskennallinen tiede Koodi: S-114

Valvoja: Prof. Jukka Tulkki

Ohjaaja: TkT Jani Oksanen

Diplomityössä esitellään ledien toiminnan kuvauksessa käytettyjä fysikaalisia malleja sekä mallinnetaan kahden valitun ledirakenteen toimintaa numeerisesti. Mallit ratkaistaan käyttämällä hyväksi elementtimenetelmää. Mallinnettavat ledirakenteet perustuvat TFFC- ja TMJ-ledeihin, jotka on hiljattain esitelty tieteellisessä kirjallisuudessa tehokkaina valaistusledirakenteina.
Diplomityössä käytetyt numeeriset mallit perustuvat Maxwellin yhtälöihin, Fermi-Dirac-statistiikkaan, puolijohteiden virrankuljetusyhtälöihin ja yleisiin rekombinaatiomalleihin. Työssä mallinnetaan nitridipuolijohteita, joissa esiintyy voimakkaita spontaaneja sekä pietsosähköisiä polarisaatiokenttiä, ja näiden kenttien vaikutus on huomioitu työssä käytetyissä malleissa.
Työssä verrataan yllämainittuja ledirakenteita toisiinsa tutkimalla sähkövirran injektiota, ledien hyötysuhdetta, säteilevän valon tehoa sekä säteilevän valon taajuusjakaumaa. Työssä tutkitaan myös virranlevityskerroksen leveyden vaikutusta rakenteiden tehokkuuteen. Lisäksi tarkastellaan spontaanin ja pietsosähköisen polarisaation vaikutusta ledien toimintaan ja hyötysuhteeseen.

Avainsanat: Puolijohdevalaistus, ledit, nitridipuolijohteet, TFFC-ledit, TMJ-ledit, hyötysuhde, numeerinen mallinnus, FEM

# Preface

The work presented in this thesis has been carried out in the Department of Biomedical Engineering and Computational Science (BECS) at Aalto University. It has been supported by the Multidisciplinary Institute of Digitalisation and Energy, Finland.

I would like to express my warmest gratitude to my supervisor, Professor Jukka Tulkki, for giving me the interesting opportunity to work in his research group. Above all I want to thank my instructor Jani Oksanen for the inspiring and demanding guidance he has given me throughout the process of this thesis. I am also very grateful to everyone in our research group for offering a nice and motivating working environment.

Finally, I would like thank my family for all the invaluable support they have given me throughout the years. That support cannot be overrated.

Otaniemi, 4.10.2010

Pyry I. Kivisaari

# Contents

# Symbols and abbreviations

## Symbols

| | |
|---|---|
| $a$ | Lattice constant |
| $A$ | SRH recombination coefficient |
| $B$ | Radiative recombination coefficient |
| $C$ | Auger recombination coefficient |
| $c$ | Speed of light in vacuum |
| $\mathbf{D}$ | Electric displacement field |
| $D_{n,p}$ | Diffusion constants for electrons and holes |
| $\vec{\mathcal{E}}$ | Electric field |
| $E$ | Energy |
| $E_F$ | Fermi level |
| $E_g$ | Band gap between conduction and valence bands |
| $e_{33}$, $e_{31}$ | Piezoelectric constants |
| $\varepsilon_0$ | Vacuum permittivity |
| $\varepsilon$ | Permittivity |
| $\varepsilon_r$ | Relative permittivity |
| $f(E)$ | Fermi-Dirac distribution |
| $\mathcal{F}_{1/2}$ | Fermi-Dirac integral of the order 1/2 |
| $g(E)$ | Electronic density of states |
| $\hbar$ | Reduced Planck's constant |
| $\mathbf{J}$ | Current density |
| $\mathbf{k}$ | Wavevector |
| $I$ | Electric current |
| $k_B$ | Boltzmann's constant |
| $m$ | Electron mass |
| $m^*_{e,h}$ | Effective masses for electrons and holes |
| $\mu$ | Mobility |
| $n$ | Electron density |
| $N_a$ | Acceptor density |
| $N_c$ | Conduction band effective density of states |
| $N_d$ | Donor density |
| $N_v$ | Valence band effective density of states |
| $\eta_k$ | Strain in the direction of axis $k$ |
| $p$ | Hole density |
| $\mathbf{P}$ | Polarization vector |
| $\mathbf{P}_{pz}$ | Piezoelectric polarization vector |
| $\mathbf{P}_{sp}$ | Spontaneous polarization vector |
| $\mathbf{P}_{tot}$ | Total built-in polarization |
| $\phi$ | Electrostatic potential |
| $\phi_n$ | Quasi-Fermi potential for electrons |
| $\phi_p$ | Quasi-Fermi potential for holes |
| $\psi$ | Particle wavefunction |
| $q$ | Elementary charge |
| $\mathbf{r}$ | Position vector |

| | |
|---|---|
| $R$ | Recombination rate |
| $\sigma$ | Conductivity |
| $T$ | Temperature |
| $\tau$ | Recombination lifetime |
| $\Theta$ | Luminous flux |
| $V(\mathbf{r})$ | Potential energy |
| $V_a$ | Applied voltage |
| $\omega$ | Angular frequency |
| $\chi$ | Electron affinity |

## Abbreviations

| | |
|---|---|
| CSL | Current spreading layer |
| DOS | Density of states |
| EBL | Electron blocking layer |
| EQE | External quantum efficiency |
| EXE | Extraction efficiency |
| FEM | Finite element method |
| FC | flip-chip |
| INJ | Injection efficiency |
| IQE | Internal quantum efficiency |
| LED | Light-emitting diode |
| MQW | Multi-quantum well |
| PDE | Partial differential equation |
| QW | Quantum well |
| SRH | Shockley-Read-Hall |
| SSL | Solid-state lighting |
| TFFC | Thin-film flip-chip |
| TMJ | Transverse multi-quantum well junction |

## Symbols appearing as subindices

| | |
|---|---|
| $c$ | Conduction band |
| $v$ | Valence band |
| $e$, $n$ | Electron |
| $h$, $p$ | Hole |
| $a$ | Acceptor |
| $d$ | Donor |

# 1 Introduction

Improving energy efficiency is one of the key means to reduce greenhouse emissions and to enable sustainable economic growth. For example, the EU has agreed to cut its primary energy consumption by 20 % by 2020, and designing more efficient lighting for commercial and residential buildings is mentioned as one of the primary ways to achieve this goal [1]. Artificial lighting is globally one of the main users of electrical energy. In 2001, lighting was estimated to hold 22 % of the total electricity consumption in the US and approximately half of this consumption was caused by the lighting of commercial buildings. Currently the most used light sources are still the traditional incandescent light bulbs, fluorescent lamps and high-intensity discharge (HID) lamps [2].

Solid-state lighting (SSL) based on semiconductor light-emitting diodes (LEDs) is becoming a more and more viable alternative as a highly-efficient lighting technology. Whereas the efficiencies of the traditionally used lighting technologies have reached the upper limits of their potential, the efficiencies of the LED lamps have increased tremendously since the introduction of the first blue LEDs in the early 1990's, and this trend is still continuing. Conversion efficiencies from electrical energy to white light are estimated to reach 50 % within the next few years for commercial LEDs, and no physical reason restricts even higher conversion efficiencies to be reached [3, 4]. So far, commercially available white LED lamps have already achieved luminous efficacies comparable to those of fluorescent lamps. The potential of solid-state lighting is also seen in the intense experimental research conducted on them all over the world.

In addition to experimental methods, computational modeling is a vital tool in the LED research and development. With accurate numerical modeling, new highly efficient LED structures may be efficiently designed. The efficient computational research of LEDs has in part been made possible with the availability of extensive computational resources. However, a vital requirement for accurate and efficient modeling of LED structures is the knowledge of working physical models and accurate material parameter estimates. This is especially true for semiconductor nanostructures, where fundamental quantum-mechanical phenomena take place.

In this thesis, a macroscopic physical model for the current transport and electrical characteristics of semiconductor structures is constructed. The model is based on Maxwell's equations, semiconductor transport equations, Fermi-Dirac statistics and basic recombination models. A corresponding model is also presented e.g. in Ref. [5], with a good description also about the numerical implementation of the model. The semiconductor current equations are solved with *COMSOL Multiphysics*, which is a numerically powerful software for solving partial differential equations using the Finite element method (FEM).

The structures modeled in this thesis are 2-dimensional projections of two different recently introduced highly-efficient LED structures designed for white light generation, both based on group III nitride material compositions. One of them (the TFFC LED) is already commercially available by *Philips Lumileds* Corporation and the other one (the TMJ LED) is a recently proposed alternative for white

light generation. The aim of this thesis is to compare these structures with each other and to see if the TMJ LED would offer notable benefits compared with the commercially used TFFC LED. The results are also compared with the values found in the literature to check the accuracy of the used models and material parameters. In the calculations, the active region of the LEDs consists of two emitting quantum wells, one of them emitting blue and the other one emitting green light. Such a structure is chosen to study the general feasibility of direct white light generation without the use of phosphors.

The structure of this thesis is the following. Basic semiconductor physics is first reviewed in Chapter 2 with emphasis on carrier dynamics, carrier recombination and dissipation effects. In Chapters 3, 4 and 5, common structures and properties of semiconductor light emitting diodes and different LED technologies are reviewed. Special attention is paid on gallium nitride based material systems where interesting fundamental phenomena like strong intrinsic piezoelectric and spontaneous polarization fields take place. The origins of these polarization fields and their effects on LED operation are discussed as well. Solving nonlinear semiconductor transport models with Finite Element Method is briefly discussed in Chapter 6, and the results are presented in Chapter 7.

# 2 Semiconductor Physics

To understand the semiconductor current transport studied numerically in this thesis, it is necessary to be able to quantitatively describe the carrier distribution and the carrier dynamics in semiconductors. This Chapter reviews the prerequisities used later in this work.

## 2.1 Dispersion relation and density of states (DOS)

Semiconductors are solid-state materials with a periodic crystal structure. This means that atoms forming the semiconductor crystal are bound to well-defined lattice sites which repeat periodically and hence form a periodic crystal lattice. The properties of electrons on the outermost atomic orbitals are strongly affected by the periodic potential created by the lattice: the electronic states become free-electron like and their energies form a quasi-continuum with bands of allowed and bands of disallowed energy values.

Electronic states in semiconductors are essentially derived from the time-independent Schrödinger's equation:

$$\left(\frac{-\hbar^2}{2m}\nabla^2 + V(\mathbf{r})\right)\psi(\mathbf{r}) = E\psi(\mathbf{r}), \tag{1}$$

where $\psi(\mathbf{r})$ is the electron wavefunction, $E$ is the electron energy and $V(\mathbf{r})$ is the potential energy. The potential energy has the same periodicity as the crystal lattice so that $V(\mathbf{r}+\mathbf{a}) = V(\mathbf{r})$, $\mathbf{a}$ being the lattice atom separation. It can be shown that in this case, the electron wavefunctions satisfy [6]

$$\psi(\mathbf{r}) = e^{i\mathbf{k}\cdot\mathbf{r}}u_{\mathbf{k}}(\mathbf{r}), \tag{2}$$

where $u_{\mathbf{k}}(\mathbf{r})$ has the same periodicity as the potential energy. This is the Bloch theorem for particles in a periodic potential. It can be seen that the wavefunction is the same as for free electrons apart from the periodic part $u_{\mathbf{k}}(\mathbf{r})$, where $\mathbf{k}$ is the electron wavevector. The Bloch theorem can be used to show that in a periodic potential the allowed electron energies $E(\mathbf{k})$ form a quasi-continuum with allowed and disallowed bands. A nice and analytic example can be constructed by using e.g. the Kronig-Penney model in which the potential profile is composed of periodically repeating potential wells [7].

When calculating bandstructures, one constructs the dispersion relation $E(\mathbf{k})$ for all the allowed bands. Dispersion relation can be solved with various methods that model the interaction of electrons with the crystal lattice, e.g. the tight binding method, the orthogonalized plane wave method and the pseudopotential method [6]. The dispersion relation of GaN is shown in Fig. 1, calculated with the pseudopotential method neglecting spin-orbit interaction. The highest completely occupied band is commonly known as the valence band and the lowest empty or only partially occupied band is known as the conduction band.

Usually we are interested only in the wavevector region near the band edges, i.e. near the band energy minima and maxima since the optical interband transitions

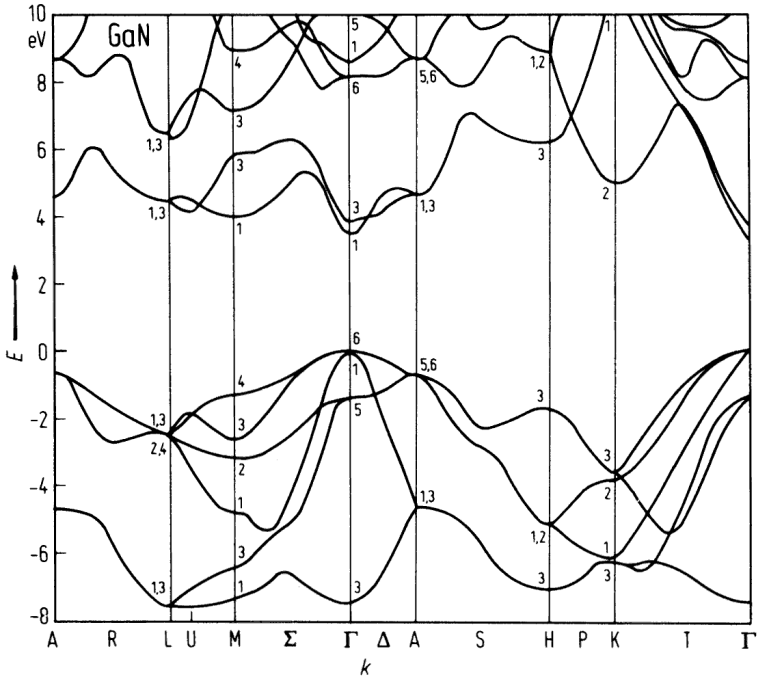


Figure 1: Dispersion relation of GaN calculated with the pseudopotential method neglecting spin-orbit interaction. GaN is a direct-gap semiconductor which means that the valence band maximum and the conduction band minimum occur at the same point in **k**-space. Band gap between the conduction and valence bands is 3.39 eV at Γ point which stands for $\mathbf{k} = 0$. The figure is reproduced from Ref. [8].

and current transport take place there. Bandstructure near the band edges may be calculated with the $\mathbf{k} \cdot \mathbf{p}$ method or in the simplest approximation, as a simple parabolic relation with help of the concept of effective mass.

In this thesis, the parabolic band approximation is used for approximating the dispersion relation. In the parabolic approximation, the dispersion relation is

$$E(\mathbf{k}) = E_{c,v} + \sum_{i=1}^{3} \frac{\hbar^2 k_i^2}{2m^*_{c,v,ii}}, \tag{3}$$

where $E_c$ is the conduction band minimum, $E_v$ is the valence band maximum and $m^*_{c,v,ii}$ are the effective masses for electrons in the conduction band and the valence band in the three orthogonal **k** directions, respectively. Effective masses are generally defined as a 3x3 tensor:

$$[m^*]_{ij} = \hbar^2 \frac{1}{\nabla_{k_i} \nabla_{k_j} E(\mathbf{k})}. \tag{4}$$

Note that for states close to maxima of the dispersion relation, the effective mass becomes negative. In these regions it is often useful to introduce the concept of a hole, i.e. a quasiparticle that corresponds to an empty electronic state. The holes in

the valence band behave just as the valence band electrons, except that the charge and the effective mass of holes are positive.

The density of states (DOS) describes the number of available electronic states for a particular energy value, i.e. $g(E) = dn/dE$, where $dn$ is the number of states in the interval $dE$ (per unit volume). By using the parabolic dispersion relation, the conduction and valence band densities of states for 3-dimensional bulk material may be approximated as

$$g_c(E) = \frac{1}{2\pi^2}\left(\frac{2m_c^*}{\hbar^2}\right)^{3/2}\sqrt{E - E_c} \tag{5}$$

for the conduction band and

$$g_v(E) = \frac{1}{2\pi^2}\left(\frac{2m_v^*}{\hbar^2}\right)^{3/2}\sqrt{E_v - E} \tag{6}$$

for the valence band. Here the effective mass tensors are replaced by scalar values. The double degenerate valence band (heavy and light holes) is also represented by a single effective mass.

Quantum wells (QWs) are material layers where one of the dimensions is on the order of the de Broglie wavelength for electrons. In QWs, the electronic states are quantized in the direction perpendicular to the QW layer. The density of states is calculated by first solving the discrete values for the perpendicular wave vector component $k_\perp$ and the corresponding energy values from Schrödinger's equation. After that, the density of states is solved separately for each discrete $k_\perp$ value. By using the parabolic approximation it can be shown that the density of states is constant for each subband assigned by the values of $k_\perp$. The conduction band densities of states for 3D bulk material and a 2D quantum well are compared in Fig. 2.

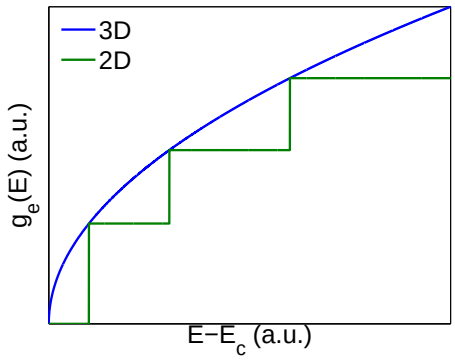


Figure 2: Conduction band density of states for a 3D bulk material and a 2D quantum well.

## 2.2 Carrier distribution

In thermal equilibrium the occupation probability of an electronic state with energy $E$ is given by the Fermi distribution:

$$f(E) = \frac{1}{\exp\left(\frac{E-E_F}{k_B T}\right) + 1}, \tag{7}$$

where $E_F$ is the Fermi level for electrons. The density of states for holes is the common valence band density of states written in Eq. (6) but the distribution function is the complement of the Fermi distribution, i.e. $1 - f(E)$ [9]. The carrier density in an energy band can be calculated from the DOS and the occupation probability as

$$n^{band} = \int_{band} g(E) f(E) dE. \tag{8}$$

In intrinsic semiconductors, the Fermi level is located in the forbidden energy gap (commonly known as the band gap) between the conduction and valence bands. As a consequence, the occupation probability is $f(E) = 1$ for valence band states and $f(E) = 0$ for conduction band states at $T = 0\,K$.

As can be seen from Eq. (8), electrons start to excite from the valence band to the conduction band at positive temperatures. As a consequence, the conduction band becomes partially filled, the valence band is no longer completely filled and both bands start to conduct. The forming and calculation of conduction band electron density and valence band hole density are depicted in Fig. 3.

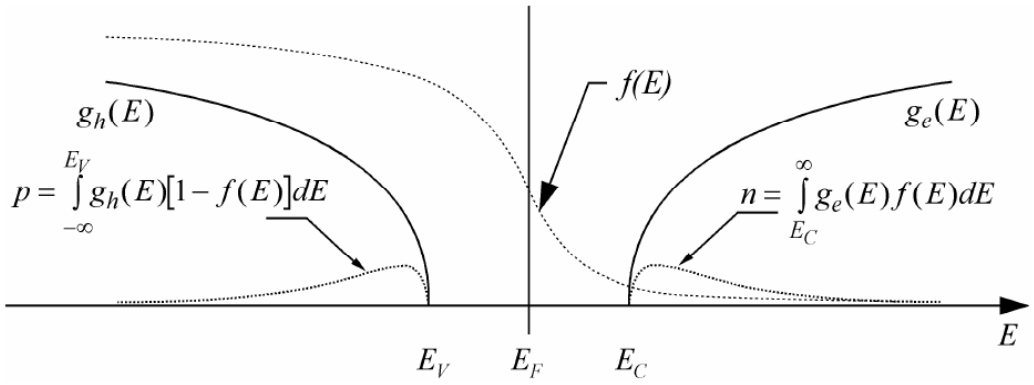


Figure 3: Fermi distribution, densities of states and electron and hole densities in an intrinsic semiconductor. The figure is reproduced from Ref. [9].

In thermal equilibrium the Fermi level is common to both the conduction and the valence band. Under excitation of light or electric current, the Fermi level is divided into quasi-Fermi levels for the conduction band electrons and the valence band holes. Solving the values for the quasi-Fermi levels is part of the semiconductor current model presented in Section 2.3.

Numerical implementation of semiconductor carrier statistics is straightforward if one makes use of the Fermi-Dirac integral of the order 1/2, defined as

$$\mathcal{F}_{1/2}(\eta) = \frac{1}{\Gamma(3/2)} \int_0^\infty \frac{x^{1/2} dx}{1 + e^{(x-\eta)}}, \tag{9}$$

where $\Gamma$ is the Gamma function. Eq. (9) may be implemented as a numerical table, knowing that $\Gamma(3/2) = \sqrt{\pi}/2$ [10]. With the parabolic density of states, Eq. (8) for conduction band electrons and a similar equation for valence band holes may be recast in the form

$$n = N_c \mathcal{F}_{1/2} \left( \frac{E_{Fn} - E_c}{k_B T} \right) \tag{10}$$

$$p = N_v \mathcal{F}_{1/2} \left( \frac{E_v - E_{Fp}}{k_B T} \right), \tag{11}$$

where $E_{Fn}$ and $E_{Fp}$ are the quasi-Fermi levels for electrons and holes and $N_c$ and $N_v$ are the effective conduction and valence band densities of states, defined as

$$N_c = 2 \left( \frac{m_e^* k_B T}{2\pi\hbar^2} \right)^{3/2} \text{ and } N_v = 2 \left( \frac{m_h^* k_B T}{2\pi\hbar^2} \right)^{3/2}. \tag{12}$$

### 2.2.1 Boltzmann approximation

Boltzmann approximation is an asymptotic approximation for Fermi-Dirac statistics that is used in many simplifying analytic models in this thesis. In the approximation, the Fermi distribution is replaced by the Boltzmann distribution, resulting in

$$n = N_c e^{(E_{Fn} - E_c)/k_B T} \tag{13}$$

$$p = N_v e^{(E_v - E_{Fn})/k_B T}. \tag{14}$$

To illustrate the applicability of the Boltzmann approximation, the Fermi integral of the order 1/2 and the Boltzmann exponential are plotted in Fig. 4. It is seen that the Boltzmann approximation is good for $E_c - E_{Fn} >> k_B T$ or $E_{Fp} - E_v >> k_B T$, i.e. when the quasi-Fermi levels are deep within the band gap. Boltzmann approximation can also be used for doped semiconductors (see the next section) as long as the doping densities are smaller than the effective densities of states.

### 2.2.2 Doping of semiconductors

One of the technologically essential properties of semiconductors is the ability to dope them with impurity atoms. This means replacing atoms in the crystal by impurity atoms that become easily ionized at finite temperatures. Donors are atoms that can release one electron to the conduction band and acceptors are atoms that

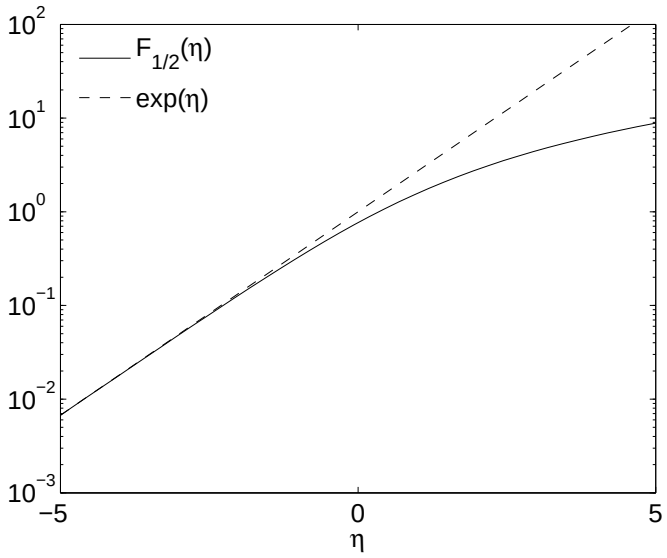


Figure 4: Fermi integral of the order 1/2 and its exponential approximation as a function of $\eta = (E_{Fn} - E_c)/k_BT$ or $\eta = (E_v - E_{Fp})/k_BT$. The approximation $\mathcal{F}_{1/2}(\eta) = e^{\eta}$ holds if $\eta << 0$.

can bind one electron from the valence band. As a result, extra carriers are created in the semiconductor material.

The donors release additional electrons into the conduction band, so that the density of ionized acceptors is given by

$$N_d^+ = n_{add}, \tag{15}$$

where $n_{add}$ is the density of additional conduction band electrons. The density of nonionized donors in the Boltzmann approximation is given by

$$N_d - n_{add} = N_d^0 = g_d N_d e^{-(E_d - E_F)/k_BT}, \tag{16}$$

where $N_d$ is the total donor density, $N_d^0$ is the density of nonionized donors, $g_d$ is the donor state degeneracy and $E_d$ is the donor state energy. The density of additional electrons is assumed to be much greater than the electron density of an intrinsic semiconductor so that $n_{add} \approx n$. With this approximation we can use Eq. (13) for the additional electron density. By expanding the right-hand side of Eq. (16) with $n$ we get

$$N_d - n = g_d N_d \frac{n}{N_c} e^{(E_c - E_d)/k_BT}. \tag{17}$$

Rearranging terms gives the electron density in a semiconductor doped with donor atoms:

$$n = \frac{N_d}{1 + g_d \frac{N_d}{N_c} e^{(E_c - E_d)/k_BT}}. \tag{18}$$

Eq. (18) shows that practically all the donors have released an electron into the conduction band if the ionization energy $E_c - E_d$ is small and the density of donor atoms is significantly smaller than the effective density of states for the conduction band.

A corresponding equation may be derived for the hole density in a semiconductor doped with acceptors:

$$p = \frac{1}{1 + g_a \frac{N_a}{N_v} e^{(E_a - E_v)/k_B T}}, \tag{19}$$

where $N_a$ is the acceptor density, $g_a$ is the acceptor state degeneracy and $E_a$ is the acceptor state energy. Again the hole density is the same as the acceptor density if the ionization energy is small and the acceptor density is significantly smaller than the valence band effective density of states.

Formulas (18)-(19) hold when the Fermi level is well below (above) the donor (acceptor) energy state. This range can be expanded using the Fermi distribution in Eq. (16). The results are slightly more complicated than the ones in Eqs. (18), (19) but they hold also outside the application range for the Boltzmann approximation, i.e. when $E_F$ is close to $E_d$ or $E_a$.

Materials doped with donor atoms are commonly called n-type and materials doped with acceptor atoms are commonly called p-type. For most semiconductors, there are suitable donor and acceptor materials for which the ionization energy is small and the dopants are ionized, creating free carriers in the material. In group III nitrides, however, the acceptor activation remains low because of the high acceptor ionization energies and the presence of hydrogen impurities. Nitride acceptor activation is discussed in more detail in Section 4.2.

In this thesis, special attention is paid on group III nitrides. For this reason, the shallow donor and acceptor levels including vacancies are listed in tables 1 and 2 for AlN, GaN and InN with the corresponding ionization energies. It can be seen that none of the acceptor ionization energies is less than $10^{-1}$ eV.

Table 1: Shallow donor levels and corresponding ionization energies in group III nitrides [11]. Si is the most commonly used donor material.

| Material | Donor | Ionization Energy (eV) |
|---|---|---|
| AlN | Vacancy in N site | 0.17 |
| | C in Al site | 0.2 |
| GaN | Si in Ga site | $0.012 - 0.02$ |
| | Vacancy in N site | 0.03 |
| InN | Vacancy in N site | $< 0.04$ |

## 2.3 Current transport in semiconductors

In this thesis, semiconductor current is modeled by a macroscopic model based on the drift-diffusion equations for current transport, the Poisson equation for electrostatic

Table 2: Shallow acceptor levels and corresponding ionization energies in group III nitrides [11]. Mg is the most commonly used acceptor material.

| Material | Acceptor | Ionization Energy (eV) |
|---|---|---|
| AlN | Mg in Al site | 0.1 |
| | Zn in Al site | 0.2 |
| GaN | Mg in Ga site | $0.14 - 0.21$ |
| | Zn in Ga site | 0.21 |
| | Vacancy in Ga site | 0.14 |

potential and the continuity equations for electrons and holes derived from the Maxwell's laws. In the model the electrostatic potential is solved from Poisson's equation:

$$\nabla \cdot \mathbf{D} = q(p - n + N_d^+ - N_a^-), \tag{20}$$

where $\mathbf{D}$ is the electric displacement field, $N_d^+$ is the density of ionized donors and $N_a^-$ is the density of ionized acceptors. Electric displacement field may be expressed by the electric field $\vec{\mathcal{E}}$ and polarization $\mathbf{P}$ so that

$$\mathbf{D} = \varepsilon_0 \vec{\mathcal{E}} + \mathbf{P} = -\varepsilon_0 \nabla\phi + \mathbf{P}, \tag{21}$$

where $\phi$ is the electrostatic potential and $\varepsilon_0$ is the permittivity of vacuum. In general, semiconductor materials have both built-in polarization fields and polarizations induced by the electric field. Polarizations induced by the electric field may be taken into account with relative permittivity $\varepsilon_r$ so that

$$\mathbf{D} = -\varepsilon_r \varepsilon_0 \nabla\phi + \mathbf{P}_{int} = -\varepsilon \nabla\phi + \mathbf{P}_{int}, \tag{22}$$

where $\mathbf{P}_{int}$ includes only the built-in polarizations unaffected by the electric field. The equation for electrostatic potential is given by substituting Eq. (22) into Eq. (20). The built-in polarization fields are discussed in more detail in Section 4.4. It must also be taken into account that the band energies follow the electrostatic potential so that $E_c = E_{c0} - q\phi$ and $E_v = E_{v0} - q\phi$, where $E_{c0}$ and $E_{v0}$ are the band edges for the chosen zero potential level.

Current in semiconductors is transported both by electrons in the conduction band and holes in the valence band. The continuity equations for electron and hole currents can be derived from Ampère's law:

$$\nabla \times \mathbf{H} = \frac{\partial}{\partial t}\mathbf{D} + \mathbf{J}, \tag{23}$$

where $\mathbf{H}$ is the magnetic field and $\mathbf{J}$ is the total electric current. By taking the divergence of Ampère's law, we get

$$0 = \nabla \cdot (\nabla \times \mathbf{H}) = \frac{\partial}{\partial t}\nabla \cdot \mathbf{D} + \nabla \cdot \mathbf{J}. \tag{24}$$

By using Eq. (20) for the electric displacement field and assuming the number of ionized dopants to be constant in time, equation (24) can be expressed as

$$\nabla \cdot (\mathbf{J}_n + \mathbf{J}_p) + q\frac{\partial}{\partial t}(p - n) = 0, \tag{25}$$

where $\mathbf{J}$ has been divided into electron and hole currents $\mathbf{J}_n$ and $\mathbf{J}_p$. The equation can be rewritten as

$$-q\frac{\partial n}{\partial t} + \nabla \cdot \mathbf{J}_n = -q\frac{\partial p}{\partial t} - \nabla \cdot \mathbf{J}_p. \tag{26}$$

In Eq. (26), the left-hand side contains only $n$-dependent terms and the right-hand side contains only $p$-dependent terms. The equation can be separated by defining a new variable that must depend both on $n$ and $p$:

$$-q\frac{\partial n}{\partial t} + \nabla \cdot \mathbf{J}_n = qR(n, p), \tag{27}$$

$$q\frac{\partial p}{\partial t} + \nabla \cdot \mathbf{J}_p = -qR(n, p), \tag{28}$$

where $R$ is defined as the total recombination-generation rate with positive values of $R$ standing for a net recombination [12]. A parametrized model for $R$ will be presented in Section 2.4. In this thesis only steady-state equations are studied with the time derivatives set to zero.

The transport equations for electron and hole currents can be written separately by assuming Boltzmann approximation to hold. The currents depend on the electric field (drift current) and carrier density gradients (diffusion current) so that

$$\mathbf{J}_n = -q\mu_n n\nabla\phi + qD_n\nabla n, \tag{29}$$

$$\mathbf{J}_p = -q\mu_p p\nabla\phi - qD_p\nabla p, \tag{30}$$

where $\mu_{n,p}$ are the mobilities and $D_{n,p}$ are the diffusion constants for electrons and holes, respectively. The diffusion constants are defined by the Einstein relation so that $D_{n,p} = \frac{k_B T}{q}\mu_{n,p}$ [13]. The current equations may be simplified with help of the Boltzmann approximation and the quasi-Fermi levels. By substituting Eqs. (13) and (14) in Eqs. (29) and (30), the current densities may be expressed as

$$\mathbf{J}_n = \mu_n n\nabla E_{Fn} = -q\mu_n n\nabla\phi_n, \tag{31}$$

$$\mathbf{J}_p = \mu_p p\nabla E_{Fp} = -q\mu_p p\nabla\phi_p. \tag{32}$$

Here we have defined new scalar fields, namely the quasi-Fermi potential fields, so that $-q\nabla\phi_{n,p} = \nabla E_{Fn,p}$. Eqs. (31), (32) are more favorable to solve numerically than Eqs. (29), (30) because of a better numerical stability achieved [10]. Eqs.

(31), (32) are substituted in Eqs. (27), (28) to get the final equations for quasi-Fermi potentials. The final equation system for solving steady-state values for $\phi$, $\phi_n$ and $\phi_p$ is given by

$$\begin{cases} \nabla \cdot (-\varepsilon \nabla \phi + \mathbf{P}_{int}) = q\left(p - n + N_d^+ - N_a^-\right) \\ \nabla \cdot (-\mu_n n \nabla \phi_n) = R \\ \nabla \cdot (-\mu_p p \nabla \phi_p) = -R. \end{cases} \tag{33}$$

All the boundary conditions for Eqs. (33) may be formulated by using Dirichlet and Neumann boundary conditions. The boundary conditions for electrical contacts are Dirichlet-type, so that the boundary values of the electrostatic potential are given by the internal potential of the structure and the applied voltage. The internal potential is determined by the material compositions and doping densities of the structure as explained in Section 3.2. The boundary values of the quasi-Fermi potentials at the contacts are the same as the applied voltage values.

At semiconductor-insulator interfaces it is usually required that the electric flux and electric current outside the semiconductor vanish. This requirement results in the Neumann boundary conditions given by

$$\begin{cases} \mathbf{n} \cdot (-\varepsilon \nabla \phi + \mathbf{P}_{int}) = 0 \\ \mathbf{n} \cdot (-\mu_n n \nabla \phi_n) = 0 \\ \mathbf{n} \cdot (-\mu_p p \nabla \phi_p) = 0, \end{cases} \tag{34}$$

where $\mathbf{n}$ is the unit normal vector at the surface. Neumann boundary conditions are also applied at the interfaces between two different semiconductor regions so that

$$\begin{cases} \mathbf{n} \cdot (-\varepsilon_1 \nabla \phi_1 + \mathbf{P}_{int,1}) = \mathbf{n} \cdot (-\varepsilon_2 \nabla \phi_2 + \mathbf{P}_{int,2}) \\ \mathbf{n} \cdot (-\mu_{n,1} n_1 \nabla \phi_{n,1}) = \mathbf{n} \cdot (-\mu_{n,2} n_2 \nabla \phi_{n,2}) \\ \mathbf{n} \cdot (-\mu_{p,1} p_1 \nabla \phi_{p,1}) = \mathbf{n} \cdot (-\mu_{p,2} p_2 \nabla \phi_{p,2}), \end{cases} \tag{35}$$

where the subindices 1 and 2 refer to the two regions alongside the interface.

## 2.4 Recombination in semiconductors

Recombination is an interband relaxation process in which an electron is transferred from the conduction band to an empty state in the valence band (i.e. the electron recombines with a hole). Energy is released in the recombination process as light or as heat. The operation of LEDs is based on radiative recombination in which the energy is released in the form of light. In addition to the radiative recombination, the most notable recombination processes include the nonradiative Shockley-Read-Hall and Auger recombinations in which the energy is eventually released as heat.

The theoretical models of recombination are essentially based on the time-dependent quantum-mechanical models and the time-dependent perturbation theory. These theories can be used to derive Fermi's golden rule which can, in principle, be used to calculate the rates of the different recombination processes. The underlying theory and methods, however, are very complex and out of the scope of this thesis. Nevertheless, the different recombination mechanisms can be reliably and easily modeled with the following well known and widely used parametrized models.

The rate of radiative recombination in the parametrized model is given by

$$R_{rad} = B\left(np - n_i^2\right), \tag{36}$$

where $B$ is the radiative recombination coefficient and $n_i$ is the intrinsic carrier concentration [12]. Eq. (36) indicates that there is no radiative recombination in thermal equilibrium with zero current. The equation may be expressed with help of the quasi-Fermi potentials by applying Boltzmann statistics, so that

$$R_{rad} = Bnp\left(1 - e^{(E_{Fp}-E_{Fn})/k_BT}\right). \tag{37}$$

The numerical value for $B$ has been calculated for group III nitrides by application of interband transition matrix element decomposition by Dmitriev and Oruzheinikov [14]. The calculated values were on the order of $10^{-16}$ m$^3$/s for all material compositions.

In Shockley-Read-Hall (SRH) recombination, the carriers recombine via traps in the band gap caused by defects and impurities. The relaxation energy is released as phonons, i.e. lattice vibrations. SRH recombination is parametrized by electron and hole lifetimes so that

$$R_{srh} = \frac{np - n_i^2}{\tau_p(n + n_0) + \tau_n(p + p_0)}, \tag{38}$$

where $\tau_p$ and $\tau_n$ are the SRH lifetimes of electrons and holes which depend on trap densities and trap capture cross-sections [15]. $n_0$ and $p_0$ are the equilibrium values for electron and hole densities, respectively. It is commonly assumed that $\tau_n = \tau_p = \tau$ and the SRH recombination coefficient is defined as $A = 1/\tau$.

A significant number of band gap states usually occurs near unpassivated semiconductor surfaces. At surfaces the crystal periodicity is broken and valence orbitals form into electronic states located inside the band gap. For this reason, the semiconductor surface areas act as powerful nonradiative recombination centers and LED active regions should be located so that they are far from surfaces. Theoretical prediction of the surface states is very difficult and instead, simplifying macroscopic models are commonly used with surface emission velocities solved by fitting the models to experimental data, as in Ref. [16].

In group III nitrides, a significant number of threading dislocations is additionally created as a result of the imperfect crystal growth on a sapphire substrate. Forming of threading dislocations in nitride compounds is discussed in Section 4.3.

Auger processes are generation and recombination processes in which the electron-hole pair interacts with a third carrier. In Auger recombination processes, the relaxation energy is initially given to a third carrier which quickly releases the energy to lattice phonons, so that no photons are created in the process. In Auger generation processes, an electron-hole pair is created due to collision with an energetic third carrier. The net Auger recombination rate taking into account all the recombination and generation processes is given by

$$R_{aug} = (C_n n + C_p p)\,(np - n_i^2), \tag{39}$$

where $C_n$ and $C_p$ are the Auger recombination coefficients [12]. Usually the Auger recombination coefficients are assumed equal so that the common Auger coefficient is defined as $C = C_n = C_p$.

The total recombination rate is calculated by summing together all the three recombination processes. In this thesis the coefficients for electrons and holes are assumed to be equal so that the total recombination rate is given by

$$R = R_{srh} + R_{rad} + R_{aug} = \left[\frac{A}{n+p+n_0+p_0} + B + C(n+p)\right] np\left(1 - e^{(E_{Fp}-E_{Fn})/k_BT}\right). \quad (40)$$

Recombination parameter values for nitride compositions have been measured by photoluminescence experiments e.g. by Shen *et al.* [17]. They measured the coefficients at high current density levels and as a result, the estimates for $A$, $B$ and $C$ were on the order of $10^7$ $s^{-1}$, $10^{-17}$ $m^3s^{-1}$ and $10^{-42}$ $m^6s^{-1}$, respectively.

### 2.4.1 Effects of resistive losses on radiative recombination

Structures with large homogeneous current spreading layers are often used in LEDs aimed at general illumination applications. The resistive losses of the large current spreading layers, however, will deteriorate the device efficiency at large current densities. The resistive losses are studied analytically in this section to get an idea of their effect before performing numerical simulations.

In the Boltzmann approximation, the radiative recombination in the active region may be approximated by

$$R_r = BN_cN_ve^{-E_g/k_BT}\left(e^{qU/k_BT} - 1\right), \quad (41)$$

where $U$ is the separation of the quasi-Fermi potentials in the active region, $E_g$ is the band gap and $B$ is the radiative recombination coefficient demonstrated in Section 2.4. The approximation holds as long as $E_g - qU >> k_BT$ [18].

The effect of the lateral potential drop on radiative recombination rate in an LED structure schematically illustrated in Fig. 5 can be approximated by making use of equation (41). Assuming the LED is operated by a voltage significantly greater than $k_BT/q$ but still in the limits of the Boltzmann approximation, the radiative recombination rate at the left-side end of the diode is reduced by a factor of

$$\frac{R_r(U-\Delta U)}{R_r(U)} = \frac{e^{qU/k_BT}e^{-q\Delta U/k_BT} - 1}{e^{qU/k_BT} - 1} \approx e^{-q\Delta U/k_BT}, \quad (42)$$

when $e^{(qU-q\Delta U)/k_BT} >> 1$, $\Delta U$ being the drop in the quasi-Fermi potential separation. Eq. (42) shows that even a potential drop of $k_BT/q$ reduces the radiative recombination by a factor of approximately 2.7. When the bias voltage is smaller than the internal potential difference of the structure (see Ch. 3), the quasi-Fermi potential drop for electrons is assumed to be approximately the same as the electrostatic potential drop in the current spreading layer. In other terms, $\Delta U \approx \Delta\phi$, where $\Delta\phi$ is the electrostatic potential drop.

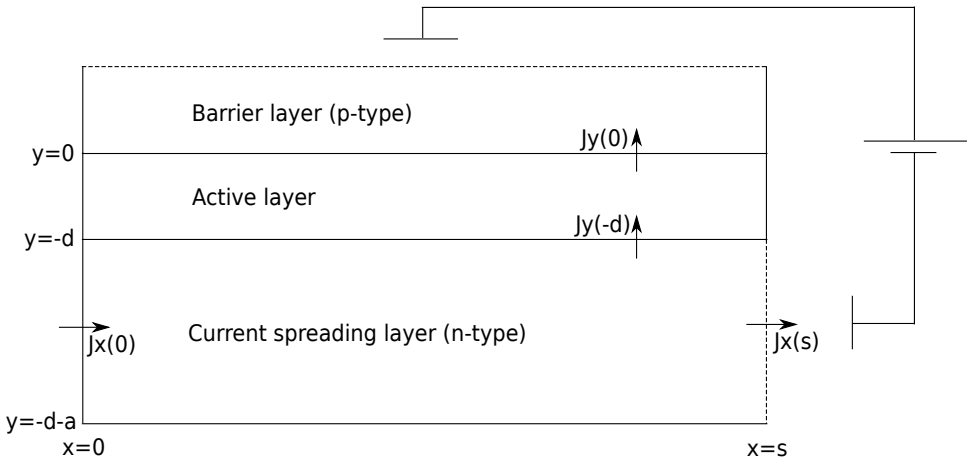


Figure 5: An outline of the parts of the LED structure essential for the treatment in this section.

In the current spreading regions, the carrier density is expected to be approximately constant so that the diffusion terms in equation (29) may be ignored. We are left with the equation for drift current:

$$\mathbf{J} = q\mu_n n\vec{\mathcal{E}} = -q\mu_n n\nabla\phi \tag{43}$$

which is essentially Ohm's law with conductivity defined as $\sigma = q\mu n$. With the very simple model of Eq. (43), the electrostatic potential drop can be estimated in the current spreading layers as a function of the current density so that

$$\phi = \phi_0 - \int \frac{1}{q\mu_n n} J_x(x)dx. \tag{44}$$

An estimate for $J_x$ can be derived by first considering the current density $J_y$ in the active region. Assuming that all electrons recombine in the active region, we can write

$$\frac{d}{dy}J_y = qR \Rightarrow J_y(-d) = \int_0^{-d} qR = -qRd \tag{45}$$

at the bottom of the active region, with $d$ being the thickness of the active region. The recombination rate is assumed to be constant throughout the active region. The total current in the $y$ direction is given by

$$I_y = \int_{act} J_y dA = -qRdWs, \tag{46}$$

where $W$ and $s$ are the lateral dimensions of the device. Assuming no recombination in the current spreading layer, the current in the $x$ direction is $I_x = -I_y$ near the contact and thus

$$J_x(s) = \frac{I_x}{Wa} = \frac{qRds}{a}, \tag{47}$$

where $a$ is the thickness of the current spreading layer.

Due to the constant current into the active region, $J_x$ diminishes linearly when moving further in the current spreading layer and it is zero at the far end of the device. Thus, the current density in the x-direction can be approximated by

$$J_x(x) = \frac{qRd}{a}x, \quad x \in (0, s). \tag{48}$$

By using Eq. (48), the potential drop can be estimated as

$$\Delta\phi = \int_0^s \frac{1}{q\mu_n n}\frac{qRd}{a}x\,dx = \frac{1}{2}\frac{Rd}{\mu_n n a}s^2. \tag{49}$$

In the structures modeled in this thesis, the dimensional values are given by $d = 20$ nm, $s = 100$ $\mu$m and $a = 2$ $\mu$m. By using this simple model with GaN material parameters and assuming $n = 10^{24}$ m$^{-3}$, the potential drop is $k_BT/q$ with a recombination rate of approximately $R = 7 \cdot 10^{31}$ m$^{-3}$s$^{-1}$. This corresponds to an optical intensity of approx. 0.6 W/mm$^2$, assuming the active region to be composed of blue-wavelength emitting InGaN. A current spreading model based on the current spreading layer resistivity and the ideal diode current law is presented in Ref. [19].

# 3 Light-emitting diodes (LEDs)

## 3.1 Semiconductor alloys

The basic elemental semiconductor materials like Silicon (Si) and Germanium (Ge) belong to the Carbon group, also known as the group IV in the periodic system of elements. All of these elements have four electrons in their outer orbitals. In addition to elemental semiconductors, binary compound semiconductors with elements from groups II, III, V and VI are widely used in semiconductor devices. Conventional III-V binary compounds include GaAs, AlAs and InP whereas ZnO is a commonly used II-VI compound. In addition, GaN is a more recently harnessed III-V binary compound for optoelectronics. All the mentioned compound semiconductors have a direct band gap making them suitable for optoelectronic applications. In contrast, both Si and Ge have indirect band gaps.

Fabrication of semiconductor alloys is an essential part of making efficient optoelectronic devices. Mixing elements from the same group to get ternary or quaternary alloys allows the engineering of band gap and lattice constant so that the emission spectrum can be tuned and material junctions can be made lattice-matched. For example, $\mathrm{In}_x\mathrm{Ga}_{1-x}\mathrm{N}$ is a ternary alloy with $x \in (0, 1)$ being the molar fraction of In. In and Ga are both group III materials and they are randomly positioned at the group III lattice sites. $\mathrm{In}_x\mathrm{Ga}_{1-x}\mathrm{As}_y\mathrm{P}_{1-y}$ is an example of a quaternary alloy with $x, y \in (0, 1)$.

Material parameters for ternary and quaternary alloys are commonly estimated by interpolating between the values measured for binary compounds. The lattice constant of a semiconductor alloy is an example of a quantity that follows a simple linear dependence on the molar fraction so that e.g. for a ternary InGaN,

$$a_{\mathrm{InGaN}} = x a_{\mathrm{InN}} + (1 - x) a_{\mathrm{GaN}}. \tag{50}$$

This is commonly referred to as Vegard's interpolation law.

Band gap is an example of a quantity that does not follow Vegard's interpolation law. An additional bowing parameter must be included that adds a quadratic component in the calculation. For example, the band gap of a ternary InGaN is calculated as

$$E_g^{\mathrm{InGaN}} = x E_g^{\mathrm{InN}} + (1 - x) E_g^{\mathrm{GaN}} + x(1 - x) b_{\mathrm{InGaN}}, \tag{51}$$

where $b_{\mathrm{InGaN}}$ is the band gap bowing parameter for InGaN [13]. As can be seen, in principle the band gap can be varied continuously between the values for binary compounds e.g. to get the desired emission wavelength.

## 3.2 pn-juntions

The most basic semiconductor LED structure is conceptually formed by joining together n- and p-type semiconductor materials as a pn-diode. Before joining the n- and p-regions together, the Fermi level values differ from each other (see Fig. 6(a)). The Fermi level gradient creates an electric current across the junction which

flattens the Fermi level. Finally the Fermi level is constant throughout the structure and an equilibrium with zero current is created (see Fig. 6(b)). In Figs. 6(a) and 6(b), $\chi$ stands for the electron affinity, i.e. the energy needed to release an electron from the conduction band to free space.

The formation of thermal equilibrium in a pn-diode can also be understood by considering the drift- and diffusion currents. After joining the n- and p-regions together, electrons diffuse from the n-side to the p-side and holes diffuse in the opposite direction. The carriers leave immobile ionized dopants on the other side of the junction and as a result, an electric field is induced across the junction. The electric field prevents further diffusion of carriers and eventually an equilibrium is created. The presence of the electric field can be seen as bending of the energy bands in Fig. 6(b).

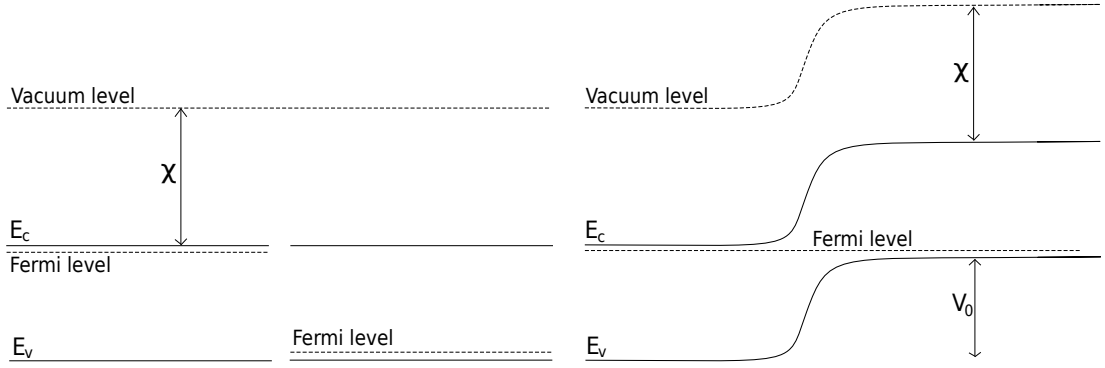


(a) pn-junction before a thermal equilibrium is reached.

(b) pn-junction in thermal equilibrium.

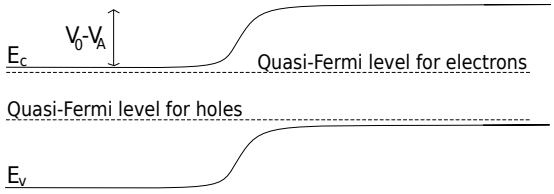


(c) pn-junction with an applied forward bias.

Figure 6: Band diagram of a pn-junction (a) before joining the regions together, (b) in thermal equilibrium after joining the regions together and (c) when a forward bias voltage is applied.

The standard method to approximate the solution of the pn-junction band diagram is the depletion region approximation. The depletion region near the junction is assumed empty of free carriers so that $n = p = 0$ in Eq. (20) and the electric field is created only by the ionized dopants. The electric field inside the depletion region is then calculated by integrating Poisson's equation:

$$\int_{-x_n}^{x} \varepsilon \frac{dE_x}{dx} = \int_{-x_n}^{x} qN_d dx \tag{52}$$

on the n-side and

$$\int_0^x \varepsilon \frac{dE_x}{dx} = -\int_0^x qN_a dx \tag{53}$$

on the p-side, with the boundary conditions

$$E_x(x_p) = E_x(-x_n) = 0, \tag{54}$$

where $x_p$ and $-x_n$ are the borders of the depletion region. The depletion approximation allows a simple analytic approximation of the built-in electric field and the depletion region width of the pn-junction. The approximation is presented in numerous textbooks, e.g. in Ref. [20] and will not be repeated in this text. The band diagram of a pn-junction may also be calculated by solving Eq. (20) numerically.

The built-in potential difference $V_0$ in a pn-junction is equivalent to the initial difference in the Fermi levels. It can be approximated by setting $n = N_d$ and $p = N_a$ deep within the homogeneous regions. By applying Boltzmann approximation on the carrier densities, the built-in potential difference is given by

$$V_0 = -\frac{E_g}{q} + \frac{k_B T}{q} \ln \frac{N_d N_a}{N_c N_v}. \tag{55}$$

When an external voltage is applied over the diode, equilibrium conditions mentioned above no longer apply and current starts to flow through the junction. In the case of a forward voltage, the potential difference between the p-side and the n-side is reduced by the applied voltage value. In this case the potential barrier at the junction interface is reduced by the amount of the applied potential making it easier for the electrons and holes to cross the junction interface (see Fig. 6(c)).

As a result of the applied voltage, the electron and hole concentrations near the interface exceed their equilibrium values and this causes a net recombination. If the total current density is high enough, radiative recombination becomes the dominating recombination process and the pn-junction emits light with a high efficiency. In the nonequilibrium situation, the Fermi level is separated into two separate quasi-Fermi levels for the conduction and valence bands.

To calculate the current density and recombination, one has to solve the drift-diffusion Eqs. (33). The highly nonlinear equations cannot be solved analytically and numerical methods are needed. It is, however, instructive to study the analytical approximation for the current of a long diode by assuming that the recombination in the depletion region can be neglected. Then the total current can be calculated by summing together the minority carrier currents on both edges of the depletion region (minority carriers are electrons on the p-side and holes on the n-side). The increase of minority carrier concentration as a function of the applied voltage may be calculated as

$$\Delta n(x_p) = n(x_p) - n_{p0} = N_d \left( e^{-q(V_0 - V_a)/k_B T} - e^{-qV_0/k_B T} \right) = n_{p0} \left( e^{qV_a/k_B T} - 1 \right) \tag{56}$$

$$\Delta p(-x_n) = p(-x_n) - p_{n0} = N_a \left( e^{-q(V_0 - V_a)/k_B T} - e^{-qV_0/k_B T} \right) = p_{n0} \left( e^{qV_a/k_B T} - 1 \right), \tag{57}$$

where $V_a$ is the applied voltage and $n_{p0}$ and $p_{n0}$ are the equilibrium minority carrier densities at the edges of the depletion region. The excess minority carriers diffuse deeper into the homogeneous regions with their diffusion velocities. Diffusion velocity for electrons is given by

$$v_n = \frac{D_n}{L_n}, \tag{58}$$

where $L_n$ is the diffusion length determined by the rate of recombination [7]. The electron current on the edge of the p-side depletion region is then

$$J_n(x_p) = q\frac{D_n}{L_n}\Delta n(x_p). \tag{59}$$

A similar equation may be derived for holes on the edge of the n-side depletion region. By summing together the currents for electrons and holes, the total current is given by an exponential law:

$$J = J_0\left(e^{qV_a/k_BT} - 1\right), \tag{60}$$

where $J_0$ depends on the diffusion constants and dopant densities in both sides of the junction:

$$J_0 = qn_i^2\left(\frac{D_n}{N_aL_n} + \frac{D_p}{N_dL_p}\right). \tag{61}$$

In the treatment, it was assumed that the quasi-Fermi levels are constant throughout the depletion region and that recombination in the depletion region is negligible.

## 3.3 Heterojunctions

Using a plain pn-homojunction as an LED is highly inefficient since the light emitted near the junction is mostly absorbed before it reaches the surface of the semiconductor and escapes. Optically more powerful devices are fabricated by making use of semiconductor heterostructures which have become a central part of semiconductor technology due to the improvements in epitaxial techniques since the 1970's [13].

In a double heterostructure LED the active light-emitting material is made of a lower band gap material than the surrounding layers. Most often the heterojunction is realized as an abrupt junction, where the material composition changes within a distance of only a few lattice constants. As a result, the band gap becomes discontinuous. A common method to estimate how the discontinuity is divided between the bands is the Anderson's affinity rule in which the conduction band discontinuity is given by $\Delta E_c = \chi_1 - \chi_2$, where $\chi_1$ and $\chi_2$ are the electron affinities on both sides of the junction [6]. However, for nitride material heterostructures modeled in this thesis, a band discontinuity ratio suggested by Karpov is used so that 70 % of the discontinuity is in the conduction band and 30 % in the valence band [21].

A numerically calculated band diagram of a double heterostructure with zero applied voltage is shown in Fig. 7(a). The material on the left is n-type, the

material on the right is p-type and the region in the middle is composed of a smaller band gap intrinsic material. The band diagram with an applied forward bias voltage is shown in Fig. 7(b). In the structure of Fig. 7(b), photons emitted in the active region are not absorbed in the cladding layers made of a wider band gap material.

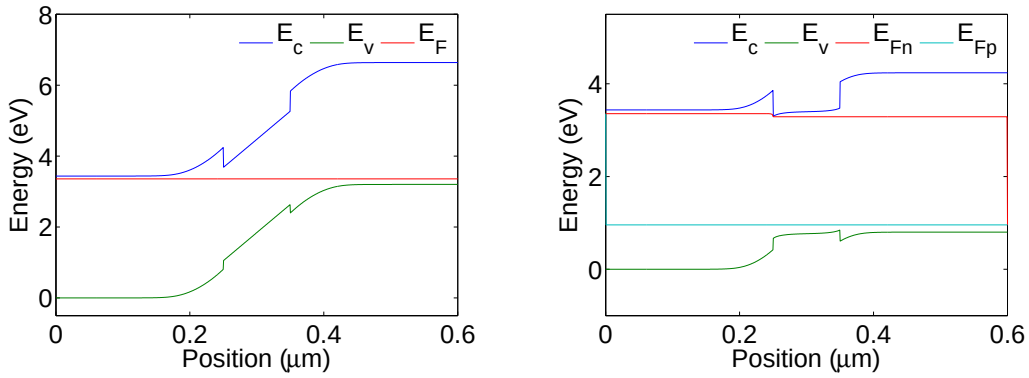


(a) Heterojunction in thermal equilibrium.

(b) Heterojunction with an applied forward bias.

Figure 7: Band diagram of a pin-heterojunction (a) in thermal equilibrium and (b) when a forward bias is applied.

## 3.4 LED efficiency

The efficiency of LEDs is affected by several physical phenomena and there are various useful figures of merit for describing the efficiency. The external quantum efficiency (EQE) is the ratio describing the number of extracted photons divided by the number of electrons flowing through the device. EQE is given by

$$\eta_{\mathrm{EQE}} = \frac{P_{opt}/\hbar\omega}{I/q}, \tag{62}$$

where $P_{opt}$ is the extracted optical power, $\omega$ is the photon angular frequency and $I$ is the total current [22]. The external quantum efficiency may be separated into internal quantum efficiency (IQE), injection efficiency (INJ) and extraction efficiency (EXE) so that $\eta_{\mathrm{EQE}} = \eta_{\mathrm{IQE}}\eta_{\mathrm{INJ}}\eta_{\mathrm{EXE}}$ [23]. The internal quantum efficiency gives the proportion of emitted photons to recombination events and is given by

$$\eta_{\mathrm{IQE}} = \frac{R_{rad}}{R_{rad} + R_{srh} + R_{aug}}. \tag{63}$$

The IQE may be approximated by studying the behavior of Eq. (40) at high carrier injection values. If we assume that $n \approx p$ and that the carrier densities are significantly higher than the equilibrium densities we can write

$$\eta_{\mathrm{IQE}} = \frac{Bn^2}{Bn^2 + \frac{1}{2}An + 2Cn^3}. \tag{64}$$

The maximum of Eq. (64) gives the highest internal quantum efficiency that may be achieved with optimal carrier densities. It is obtained by $n = \sqrt{A/4C}$ and given by

$$\eta_{\mathrm{IQE},max} = \frac{B}{B + 2\sqrt{AC}}. \tag{65}$$

Injection efficiency is the ratio of recombined electrons to all the electrons flowing through the device:

$$\eta_{\mathrm{INJ}} = \frac{\int_{act} R_{tot}\, d\mathbf{x}}{I_{tot}/q}, \tag{66}$$

where the integration is performed over the active material layer of the LED.

Extraction efficiency describes the proportion of the emitted photons that eventually escape the LED and contribute to the output power. EXE accounts for the effects like optical absorption and photon recycling, which refers to the process where photons emitted in the confined optical modes of the cavity are absorbed by the active region and re-emitted to modes in which the photons can exit the cavity. Computational estimation of EXE is challenging but it can alternatively be defined as $\eta_{\mathrm{EXE}} = \eta_{\mathrm{EQE}}/(\eta_{\mathrm{IQE}}\eta_{\mathrm{INJ}})$.

The overall efficiency $\eta_{\mathrm{TOT}}$ of an LED is calculated by dividing the total extracted optical power by the total electrical input power so that

$$\eta_{\mathrm{TOT}} = \frac{P_{tot}}{IV}. \tag{67}$$

One of the peculiarities of semiconductor LEDs is their ability to extract heat out of the semiconductor structure. The energy extracted out of the LED by a photon corresponds to the energy of the radiatively recombining electron-hole pair, which is slightly larger than the band gap energy and significantly larger than the electrical energy needed to create the photon. If photons can be extracted with a high EQE, the heat energy extracted from the system in the form of photons may cool down the LED. A thermophotonic heat pump based on this phenomenon has been recently proposed and is currently being developed [24].

### 3.4.1 Photometric efficiency figures

When designing visible light sources, the LED power must also be measured with respect to human vision. This is done by using photometric quantities which account for the human eye sensitivity. The basis for the photometric quantities is the experimentally determined human eye sensitivity function $V(\lambda)$ which models the eye response to a wavelength $\lambda$.

In the commonly used CIE 1931 standard, the eye sensitivity function has its maximum at approximately 555 nm and it is zero in the infrared and ultraviolet wavelength regions. The luminous flux of a light source is defined as the light power received by the human eye and it can be calculated by making use of the eye sensitivity function:

$$\Theta = 683\frac{\mathrm{lm}}{\mathrm{W}}\int_{\lambda} V(\lambda)P(\lambda)d\lambda, \tag{68}$$

where 683 is a normalization factor and $P(\lambda)$ is the spectral power density, so that the total radiation power is

$$P = \int_{\lambda} P(\lambda)d\lambda. \tag{69}$$

By making use of the definition for $\Theta$, the luminous efficacy can be defined as

$$\frac{\Theta}{P} = \frac{683\frac{\mathrm{lm}}{\mathrm{W}}\int_{\lambda} V(\lambda)P(\lambda)d\lambda}{\int_{\lambda} P(\lambda)d\lambda}, \tag{70}$$

with the unit 1 lm/W. Usually the lighting device performance is reported using the luminous efficiency which tells the luminous flux per electrical input power, $\Theta/(IV)$. The unit for luminous efficiency is also lm/W.

## 3.5 Lighting based on LEDs

### 3.5.1 Suitable material systems

The essential requirement for a semiconductor material to be useful in lighting is the presence of a direct band gap with a suitable width. The band gap value must be within the visible spectrum photon energies, which range approx. from 1.65 eV to 3.26 eV. The AlGaInN material system studied in this thesis suits well for making visible-spectrum LEDs, with the theoretical spread in the band gap from 0.7 eV to 6.2 eV.

The most common traditional visible LEDs are based on using AlGaAs and AlGaInP material systems, both grown on GaAs substrate. By using these material compositions, band gaps ranging from the infrared to the green region can be achieved. In AlGaInP LEDs the GaAs substrate absorbs part of the emitted light, reducing the LED efficiency. This effect has been reduced e.g. by substituting the GaAs substrate with a transparent GaP substrate [10, 25].

Another emerging technology for making visible-spectrum LEDs is based on using organic semiconductor materials. The LEDs designed this way are commonly referred to as OLEDs and they are already in commercial use in display technologies. The OLEDs are less expensive to fabricate than inorganic LEDs but so far, their efficiencies have remained smaller. However, last year Reineke *et al.* reported an OLED structure with a luminous efficiency comparable to a fluorescent tube [26]. Recently Capelli *et al.* presented an organic light-emitting transistor (OLET) with an EQE of 5 %, which is already more than two times greater than in an OLED with an identical emitting layer and more than ten times greater than in any other OLET [27].

### 3.5.2 White light generation

Conventional LEDs themselves are almost monochromatic light sources with the spread in photon energies only on the order of $k_BT$, caused by the thermal distribution. Thus, producing white light requires using dichromatic (trichromatic) sources with the active region consisting of two (three) different material compositions.

The whiteness of the light source can be approximated by using the chromaticity coordinates. Chromaticity coordinates are based on dividing the visible spectrum into three color-matching functions corresponding to the sensitivity of the cone cells in the human eye to red, green and blue colors. The color-matching functions $\overline{x}(\lambda)$, $\overline{y}(\lambda)$ and $\overline{z}(\lambda)$ for red, green and blue, respectively, are determined experimentally by comparing a monochromatic test beam and a comparison beam consisting of adjustable amounts of red, green and blue light. In the CIE 1931 standard, the function $\overline{y}(\lambda)$ is equal to $V(\lambda)$ and the maxima of $\overline{x}(\lambda)$ and $\overline{z}(\lambda)$ are approximately 600 nm and 450 nm, respectively.

If the spectral power density $P(\lambda)$ of light is known, the three tristimulus values of the radiation can be defined as

$$\begin{aligned} X &= \int_\lambda \overline{x}(\lambda)P(\lambda)d\lambda \\ Y &= \int_\lambda \overline{y}(\lambda)P(\lambda)d\lambda \\ Z &= \int_\lambda \overline{z}(\lambda)P(\lambda)d\lambda, \end{aligned} \tag{71}$$

where $X$, $Y$ and $Z$ describe how intensive red-, green- and blue-like stimulation is needed to produce light that a human observer cannot distinguish from the original light. Values for $X$, $Y$ and $Z$ are measured in watts, so that the unitless chromaticity coordinates can be defined as

$$\begin{aligned} x &= \frac{X}{X+Y+Z} \\ y &= \frac{Y}{X+Y+Z} \\ z &= \frac{Z}{X+Y+Z} = 1-x-y. \end{aligned} \tag{72}$$

It can be seen that the $z$ coordinate is determined directly from $x$ and $y$ and thus only two coordinates are needed. The $(x, y)$ chromaticity diagram is shown in Fig. 8. Large values of $x$ indicate red colors and large values of $y$ indicate green colors. Blue color is observed when both $x$ and $y$ are small. Coordinates for white light are located in the middle and coordinates for monochromatic light are located on the border of the coloured region.

Light from a single active material composition is located near the borders of the coloured region of Fig. 8 and coordinates corresponding to white light may

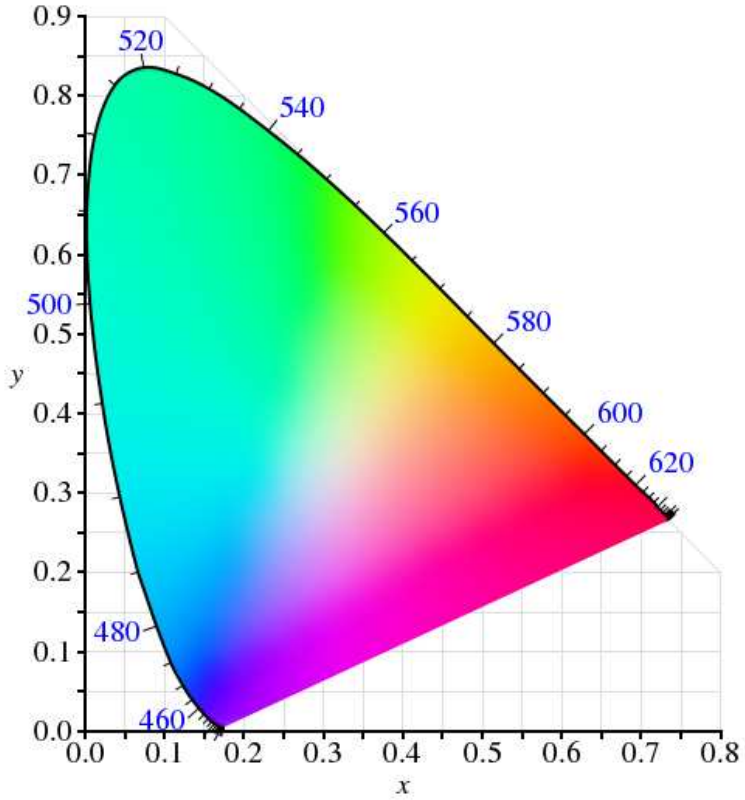


Figure 8: The chromaticity diagram according to the CIE 1931 color-mathing functions. The figure is reproduced from Ref. [28].

be achieved by combining different material compositions. In principle, white light may be generated even with two different compositions but in general, better colour rendering features are achieved by combining at least three colors. Another way of producing white light is to make use of phosphors or semiconductor wavelength converters.

# 4 Group III nitride material systems

## 4.1 Overview

Group III nitride material compositions have become increasingly important as materials for UV-, blue- and green-wavelength optoelectronic devices in the 1990's. Gallium nitride films of good quality were first succesfully manufactured in 1980's by growing them on sapphire ($Al_2O_3$) substrate, but p-type doping was still unavailable at the time [29]. The most important problems of the doping were solved by 1990's, and high-brightness nitride LEDs and nitride-based laser diodes were presented [30] [31]. Today, group III nitrides are used in numerous applications such as displays, traffic signals, Blu-ray discs and increasingly in general lighting applications [32].

The main advantage of group III nitrides is the widely tunable direct bandgap which ranges from 0.7 eV (InN) to 6.2 eV (AlN) as illustrated in Fig. 9. In principle this means that nitrides are suitable for illumination through the whole visible spectrum and even in the infrared. However, in practice it has been difficult to create high-quality InGaN or AlGaN compositions if the In or Al fraction is high due to the strong dependence of the lattice constant on the composition. The bandgaps and lattice constants for different AlGaInN compositions are shown in Fig. 9 [33].

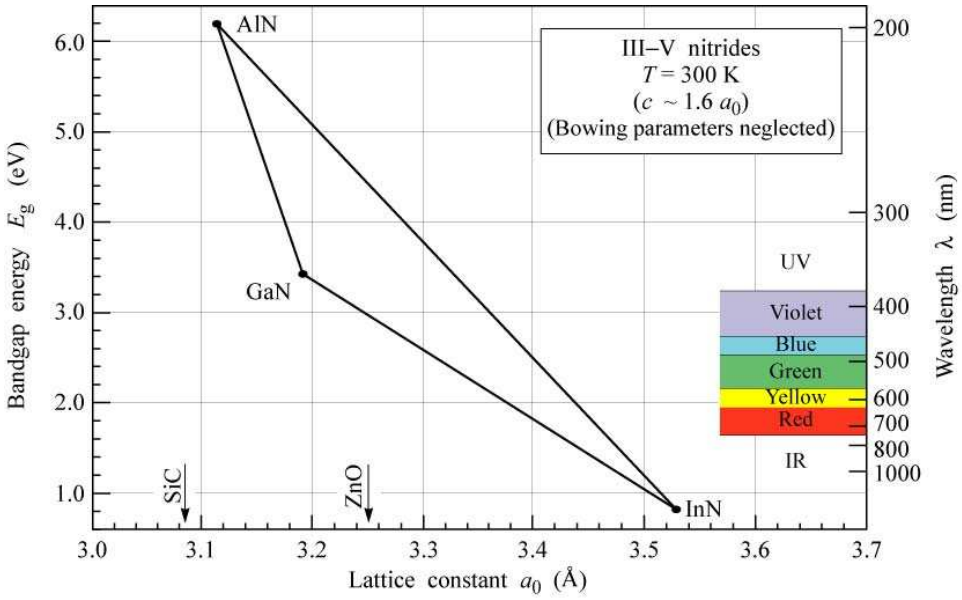


Figure 9: Bandgaps and lattice constants for AlGaInN compositions with bowing parameters neglected. The figure is reproduced from Ref. [33].

Group III nitrides grow in a wurtzite crystal structure on a sapphire substrate. The symmetry properties of wurtzite structure induce strong spontaneous and piezoelectric polarization fields which in turn create internal electric fields in nitride heterostructures. These polarizations are studied in more detail in the next section. Other problematic properties of group III nitrides include low acceptor activation

and high threading dislocation density discussed below as well.

Despite the success in developing commercially available nitride-based devices, much of the physics still remains uncharted. For further development of high-quality gallium nitride based devices, more research focused on numerical analysis is needed. In addition, the values of group III nitride material parameters and their dependencies on material composition, defect density and other physical quantities must be studied further to enable more reliable simulation of group III nitrides [32]. The effect of polarization on the physical properties of these devices also needs to be studied further. These limiting issues typical of nitrides are discussed in this section in more detail.

## 4.2 Acceptor activation

In group III nitrides, the activation energy of the acceptor atoms is large and only a few percent of the acceptor atoms are ionized at room temperature. For this reason, the acceptor density must be high in order to get a highly p-type nitride material. This, in turn, reduces the hole mobility which is already low in intrinsic group III nitrides. In gallium nitride, Mg atoms are used as acceptors.

The density of ionized acceptors $N_a^+$ may be calculated using Eq. (19) presented in Section 2.2.2 for holes. In nitride materials, the difference of $E_a$ and $E_v$ is much greater than $k_BT$ and a minority of the acceptors is ionized in room temperature. Another reason for low acceptor activation are the hydrogen atoms introduced in nitride materials during the epitaxial growth process. The hydrogen atoms share their electrons with the acceptors and no holes are created in the valence band [33].

There have been various approaches to improve nitride acceptor activation. The first one was to use the low-energy electron-beam irridation in the end of 1980's [34]. Shortly after that, Nakamura *et al.* presented acceptor-activation improvement by thermal annealing [35]. It has been suggested that by thermal annealing, the hydrogen-acceptor bond is broken and hydrogen atoms are removed from the nitride structure. In addition to these methods, the acceptor activation has been boosted by making use of AlGaN/GaN superlattices [36]. The latest approach for improving acceptor activation in nitrides is based on using the built-in polarization demonstrated in Section 4.4 [37].

## 4.3 Threading dislocations

Nitride structures are most often grown on sapphire substrate which has a corundum crystal structure, whereas group III nitrides form into a wurtzite structure. The lattice constants of sapphire and gallium nitride also differ from each other. These differences in the crystal properties create a large number of dislocations near the GaN-sapphire interface. The number of dislocations is reduced further away from the interface in the GaN-region, but some threading dislocations remain, typically on the order of $10^8$-$10^9$ cm$^{-2}$ [33]. The distribution of dislocations is sketched in Fig. 10.

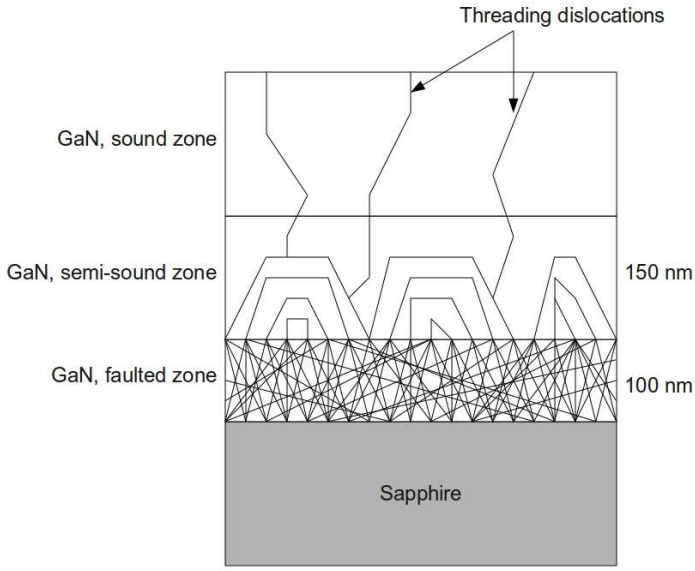


Figure 10: Dislocation density in GaN when grown on sapphire substrate. The 100 nm zone near to the interface is called the faulted zone and there the density of dislocations is high. Dislocation density is diminished when going deeper into GaN, and in the sound zone there are only threading dislocations on the order of $10^8$-$10^9$ $cm^{-2}$.

Dislocations typically introduce energy states within the band gap. These states provide a fast nonradiative recombination channel for electrons and holes. In general, the dislocations are electrically charged and also interact with free carriers either attractively or repulsively. In the case of a positively charged dislocation, electrons are attracted. Attracted electrons in turn screen the repulsive potential on holes so that the repulsion experienced by holes is reduced. However, the unfavorable effect of this process has been found to be unexpectedly small and reasons for this are still under discussion [32].

Several reasons have been suggested to explain the minor effect of threading dislocations on the internal quantum efficiency. One possible reason is that the dislocation states would lie inside the allowed bands of the semiconductor material instead of being in the bandgap [38]. This would clearly lead to the absence of non-radiative recombination. Another possible reason is the spatial variation of the bandgap due to the fluctuation in the alloy compositions [39]. In this case carriers are confined in the mimima of the bandgap where they can recombine radiatively. This mechanism is easily understood at least for ternary and quaternary alloys.

None of the reasons suggested for dislocations' minor effect on the IQE has gained general acceptance in the scientific world [33]. Even so, nitride material compositions work well for optoelectronic components despite threading dislocations. The physics of threading dislocations, however, remains a challenge for future research of group III nitride materials.

## 4.4 Internal polarizations

Group III nitride materials exhibit strong spontaneous and piezoelectric polarization that must be taken into account when modeling nitride heterostructures. These polarization fields are induced by the symmetry of the wurtzite crystal structure (spontaneous polarization) and the strain on the crystal close to the material interfaces (piezoelectric polarization). Changes in the intrinsic polarization induce surface charges on junction interfaces and generate strong electric fields in quantum well structures. The origins of these polarizations are studied qualitatively in this section and their basic effects are discussed as well.

The origins of spontaneous polarization lie in the low symmetry properties of a crystal. GaN, InN and AlN have a wurtzite crystal structure shown in Fig. 11 which lacks perfect inversion symmetry. In the wurtzite structure, the geometrical centre of electrons differs from the geometrical centre of nuclei and therefore an intrinsic spontaneous polarization field is created. The spontaneous polarization has the same orientation as the low symmetry axis of the wurtzite crystal, namely the [0001] axis [40]. This low symmetry axis is aligned with the material growth direction and is hence perpendicular to most important material interfaces.

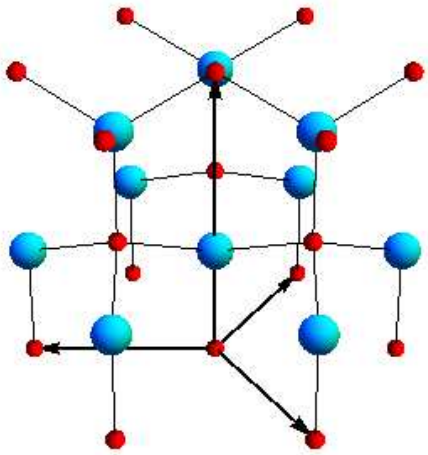

Figure 11: Wurtzite crystal structure. Vertical direction is the [0001] direction. The figure is reproduced from Ref. [42].

Another way of explaining the origins of spontaneous polarization is to look at the bonding nature of wurtzite crystal structure. The bond in [0001] direction has a different ionicity than other bonds which can also be seen as the longer length of this bond. The difference in bonding natures also shows up on the valence band structure. In wurtzite structure, the heavy hole band does not coincide with the light hole band

at Γ point [11]. These qualitative arguments show why many other common III-V semiconductors, like GaAs and InP, do not show spontaneous polarization. Most of these semiconductors have a zinc-blend structure which has a perfect inversion symmetry [41]. In nitrides, however, spontaneous polarization is a fundamental property.

Exact calculation of spontaneous polarization has been under great interest in the scientific world. Calculations have been made e.g. in Ref. [43], where results obtained by generalized gradient approximation (GGA) and local density approximation (LDA) are compared. Calculated values for spontaneous polarization in group III nitrides are presented in Table 3. The negative sign means that spontaneous polarization is antiparallel to the direction normally chosen for the [0001] axis. Interpolation laws for calculating spontaneous polarization in ternary alloys are given in Ref. [44]. Note that Vegard's law is not sufficient and a nonlinear component must be included for interpolation.

Table 3: Calculated values for spontaneous polarization and piezoelectric constants in group III nitrides [43].

| Material | $P_{sp}$ ($\mathrm{Cm}^{-2}$) | $e_{33}$ ($\mathrm{Cm}^{-2}$) | $e_{31}$ ($\mathrm{Cm}^{-2}$) |
|---|---|---|---|
| AlN | −0.090 | 1.50 | −0.53 |
| GaN | −0.034 | 0.67 | −0.34 |
| InN | −0.042 | 0.81 | −0.41 |

Piezoelectric polarization arises when the nearest neighbor bonding is altered by mechanical stress. This happens most often in abrupt heterostructures where materials of different lattice constants are joined together. In this thesis such structures are studied where different ternary alloy layers (InGaN and AlGaN) are grown on GaN substrate. In the ternary layers, atom separation as well as bonding ionicity parallel and perpendicular to the junction structure are changed differently and so a piezoelectric polarization component is created. This kind of polarization is called piezoelectric since it arises from a mechanical perturbation. Piezoelectric polarization is oriented parallel or antiparallel to spontaneous polarization, depending on whether the strain is tensile or compressive, respectively [45].

The piezoelectric polarization is a function of strains along different directions:

$$P_{pz} = e_{33}\eta_3 + e_{31}(\eta_1 + \eta_2), \tag{73}$$

where $e_{ij}$ are piezoelectric constants (see Table 3), $\eta_3$ is the strain along the [0001] direction and $\eta_1$ and $\eta_2$ are the basal strains. The strains are calculated as relative deviations from the equilibrium lattice parameters:

$$\eta_i = \frac{a_k - a_{k0}}{a_{k0}}, \tag{74}$$

where $a_{k0}$ is the equilibrium lattice parameter in the direction $k$. The basal strains $\eta_1$ and $\eta_2$ are assumed to be equal. In group III nitrides, the piezoelectric constants $e_{ij}$ are found to be about ten times larger than those of traditional III-V compounds,

making also piezoelectric polarization a fundamental part in analyzing nitride structures [46]. Piezoelectric polarization for group III nitrides may also be expressed by using only the basal strain [40]:

$$\begin{aligned} P_{pz}^{\mathrm{AlN}} &= -1.808\eta_1 + 5.624\eta_1^2 \quad \text{for } \eta_1 < 0 \\ P_{pz}^{\mathrm{AlN}} &= -1.808\eta_1 - 7.888\eta_1^2 \quad \text{for } \eta_1 > 0 \\ P_{pz}^{\mathrm{GaN}} &= -0.918\eta_1 + 9.541\eta_1^2 \\ P_{pz}^{\mathrm{InN}} &= -1.373\eta_1 + 7.559\eta_1^2. \end{aligned} \tag{75}$$

Piezoelectric polarization for ternary alloys can be approximated using the conventional Vegard's interpolation formula.

The total polarization $\mathbf{P}_{tot}$ is calculated by summing together the two polarization components:

$$\mathbf{P}_{tot} = \mathbf{P}_{sp} + \mathbf{P}_{pz}. \tag{76}$$

Total polarization in InGaN and AlGaN as a function of molar fraction is plotted in Fig. 12, assuming unstrained GaN is used as substrate.

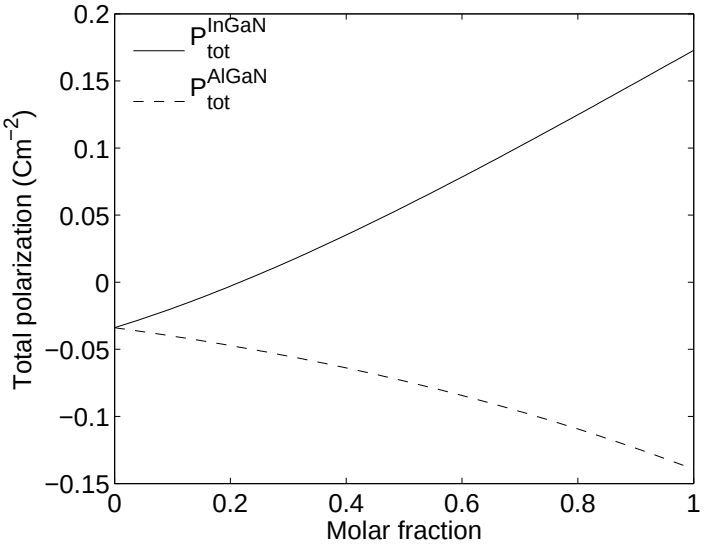


Figure 12: Total polarization of $\mathrm{In}_x\mathrm{Ga}_{1-x}\mathrm{N}$ and $\mathrm{Al}_x\mathrm{Ga}_{1-x}\mathrm{N}$ as a function of the molar fraction $x$. One can see that spontaneous and piezoelectric polarizations cancel each other out when molar fraction is approximately 0.22 in InGaN. This corresponds to a bandgap of 2.43 eV.

The effect of internal polarization field can be studied by writing down Poisson's equation (Eq. (20) in Section 2.3):

$$\nabla \cdot \mathbf{D} = q(p - n + N_d - N_a), \tag{77}$$

where the electric displacement field $\mathbf{D}$ is contributed to by the electric field and the total internal polarization:

$$\mathbf{D} = \varepsilon(-\nabla\phi) + \mathbf{P}_{tot}. \tag{78}$$

Here $\varepsilon = \varepsilon_r\varepsilon_0$ contains polarization induced by the electric field $\vec{\mathcal{E}} = -\nabla\phi$ so that $\mathbf{P}_{tot}$ consists only of the spontaneous and piezoelectric polarizations. Poisson's equation may now be written as

$$\nabla \cdot (\varepsilon(-\nabla\phi) + \mathbf{P}_{tot}) = q(p - n + N_d - N_a). \tag{79}$$

The effect of internal polarization is seen at interfaces of different semiconductor materials and at semiconductor-insulator interfaces. The boundary conditions for Poisson's equation are listed in Section 2.3, giving the Neumann boundary condition at semiconductor-insulator interface:

$$\mathbf{n} \cdot \mathbf{D} = 0, \tag{80}$$

where $\mathbf{n}$ is the unit normal vector on the surface. This implies that on the semiconductor side of the interface

$$\mathbf{n} \cdot (\varepsilon(-\nabla\phi) + \mathbf{P}_{tot}) = 0. \tag{81}$$

It can be seen that electric field must be nonzero at semiconductor-insulator interfaces. The surface electric field is induced by an equivalent surface charge density. A corresponding phenomenon occurs at interfaces of two different semiconductors. The Neumann boundary condition reads:

$$\begin{aligned} &\mathbf{n} \cdot (\varepsilon_1(-\nabla\phi_1) + \mathbf{P}_{tot,1}) = \mathbf{n} \cdot (\varepsilon_2(-\nabla\phi_2) + \mathbf{P}_{tot,2}) \\ &\Rightarrow \mathbf{n} \cdot (\varepsilon_1\nabla\phi_1 - \varepsilon_2\nabla\phi_2) = \mathbf{n} \cdot (\mathbf{P}_{tot,1} - \mathbf{P}_{tot,2}). \end{aligned} \tag{82}$$

It can be seen that if the change in polarizations is abrupt, there is also an abrupt change in electric field. This change is again caused by a surface charge density.

The effect of internal polarization may be studied with simple 1-dimensional simulations. Eq. (79) is solved numerically with FEM for a 0.6 $\mu$m long piece of intrinsic gallium nitride and Neumann boundary conditions as in equation (81) are applied in the endpoints. The band structure is shown in Fig. 13. It can be seen that there are surface charges in both ends of the structure and that an electric field is created inside the structure.

The situation is more interesting if two different nitride compositions are joined together. In this case, Neumann boundary conditions as in equation (82) are applied at the junction interface and Neumann boundary conditions as in equation (79) are applied at the endpoints. The band structure of this kind of structure is shown in Fig. 14. It can be seen that surface charges are again created on every surface. In addition, due to the significant hole concentrations on both InGaN surfaces, the band structure at the InGaN side resembles that of a p-type material.

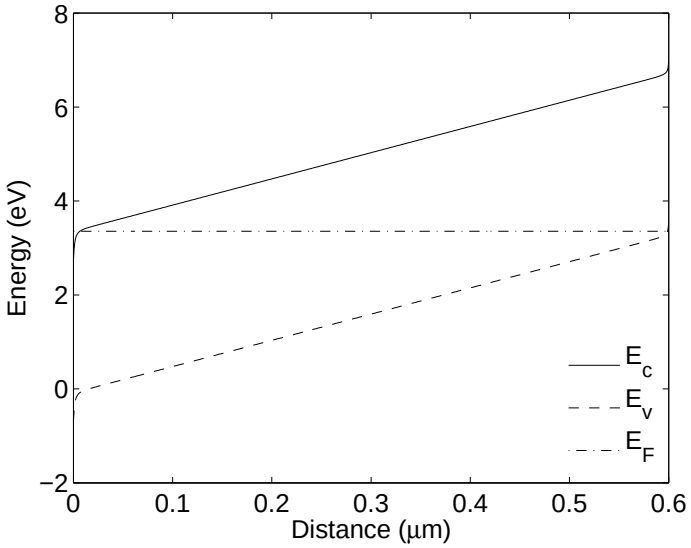


Figure 13: Band structure of intrinsic gallium nitride when Neumann boundary conditions are applied in the endpoints. It can be seen that intrinsic polarization induces surface charges in the ends and an electric field inside the structure.

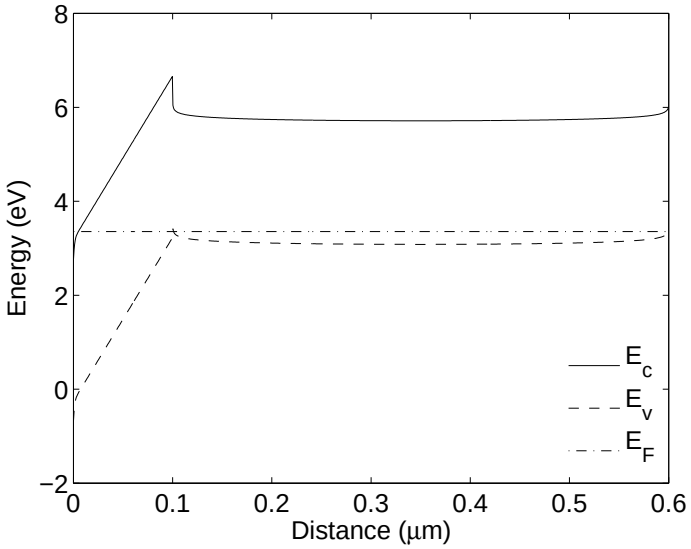


Figure 14: Band structure of a GaN-InGaN junction with Neumann boundary conditions applied at the endpoints and at the junction interface. The first 0.1 $\mu$m from the left is composed of GaN and the right side is composed of $In_{0.17}Ga_{0.83}N$. It can be seen that surface charges are induced on all interfaces and that the band structure of InGaN resembles that of a p-type material.

# 5 Some high-efficiency LED technologies

Designing an efficient high power LED device is a challenging task. The LED materials and structures affect the current injection properties, efficiency of recombination in the active material and electromagnetic mode distribution, to name only a few factors playing a role in the performance of LEDs. In addition, semiconductor manufacturing techniques set additional limitations for realizable structures. Here some examples of the most common group III nitride based structures are briefly reviewed to give an idea of the large variety of LED structures and technologies.

Simulation results for the thin-film flip-chip (TFFC) LED and the transverse multi-quantum well (TMJ) LED presented in this Chapter are given in Chapter 7.

## 5.1 Basic GaN LED structure

The basic gallium nitride LED structure is shown in Fig. 15. The sapphire substrate and the GaN buffer layer with a high dislocation density are also shown in the figure. The active multi-quantum well (MQW) region consists of a stack of InGaN QWs emitting at blue or green wavelength. On top of the active MQW region is the electron-blocking layer (EBL), a higher-band gap AlGaN layer blocking the leakage of electrons from the active material to the p-contact.

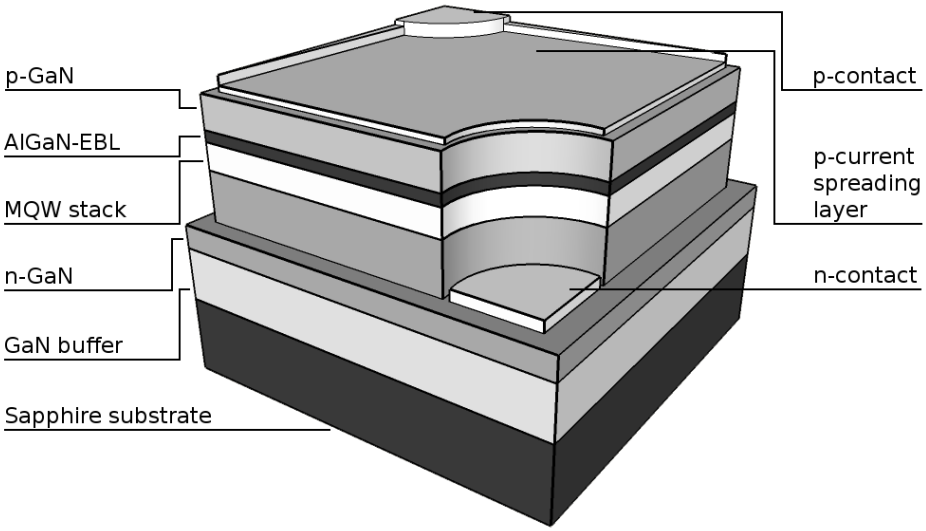


Figure 15: Basic gallium nitride LED structure. The figure is reproduced from Ref. [47].

One of the drawbacks of the basic GaN LED structure is the low extraction efficiency because of the p-type contact and wire bonding on top of the structure. This can be surpassed by using the flip-chip technology presented in Section 5.2, where the sapphire substrate is removed from blocking the light.

## 5.2 Thin-film flip-chip LEDs

The thin-film flip-chip (TFFC) LED structure is one of the most efficient technologies for lighting and already in commercial use by Philips Lumileds Lighting company, by whom it is also developed [48]. The basic unit of a TFFC LED studied in this thesis is shown in Fig. 16. In the structure, electrons and holes are injected vertically in the InGaN-MQW active region and the p-type contact is made to cover the whole LED to inject the current homogeneously through the structure. The actual LED is made by connecting multiple basic units together to form a structure with an approximately 1 $mm^2$ wide surface area [49].

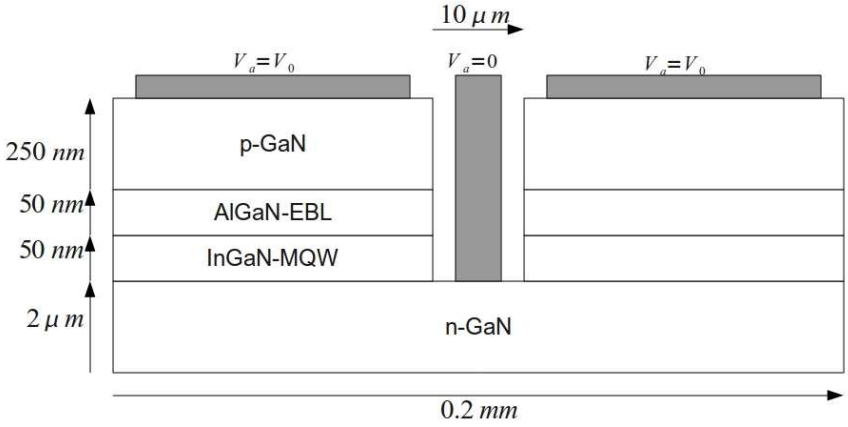


Figure 16: 2-dimensional cross-section of the basic unit of TFFC LED. The actual LED is made by connecting multiple basic units together.

The TFFC LED is made by first growing the GaN, InGan and AlGaN layers with a gold contact on a sapphire substrate. The sapphire substrate is then removed by an excimer laser and the surface facing the n-GaN layer (lowest vertical surface in Fig. 16) is roughened photoelectrochemically. This is done to reduce the number of guided modes in the semiconductor structure so that more emitted photons are extracted. The essential benefits of the TFFC LED technology are the high output power as well as the possibility for high packing density [49, 50].

The efficiencies of a TFFC LED emitting at blue wavelength and a TFFC-based white light LED lamp were studied experimentally in Ref. [49]. TFFC LEDs were found to be substantially more efficient than the basic GaN LEDs presented in Section 5.1. Experimentally measured efficiencies and output powers for a blue wavelength emitting TFFC LED are shown in Table 4 for 350 mA and 1 A injection currents. It can be seen that the external quantum efficiency decreases as the forward current increases. Corresponding photometric figures for a TFFC-based white light LED lamp are shown in Table 5.

### 5.2.1 Philips LUXEON REBEL LEDs

LUXEON REBEL by Philips Lumileds is a commercially available white light solid-state lamp that is based on thin-film flip-chip LED technology. It was selected as

Table 4: Experimentally measured output power and EQE of a TFFC LED emitting at blue wavelength [49].

| Current (mA) | Light output (mW) | EQE |
|---|---|---|
| 350 | 372 | 0.38 |
| 1000 | 875 | 0.31 |

Table 5: Experimentally measured luminous efficiency of a TFFC-based white light LED lamp [49].

| Current (mA) | Luminous efficiency (lm/W) |
|---|---|
| 20 | 96 |
| 350 | 60 |
| 1000 | 41 |

one of the EDN Hot 100 products of the year 2009, being the only high power LED to receive the award [51]. Today, Luxeon Rebel LEDs are used e.g. for street lights and general illumination. They reach luminous efficacies of over 100 lm/W at drive current values that are relevant for LEDs operating at high powers [52].

## 5.3 Transverse MQW junction LEDs

Recently Guol *et al.* proposed a new LED structure they call the Transverse multi-quantum well junction (TMJ) LED [53, 54]. A two-dimensional cross-section of its basic unit is shown in Fig. 17. In this structure, the active MQW region starts near the n-type contact so that electrons are injected in the quantum wells horizontally as well as vertically. This is expected to distribute the carriers more evenly in the quantum wells.

Efficient operation of each quantum well independent of the band gap could enable white light generation easily by using both blue- and green-emitting quantum wells in the MQW region [54].

## 5.4 Resonant-cavity LEDs

In all LED structures, the extraction efficiency (EXE) is one of the main factors limiting the LED performance. Due to the difference in refractive indices between conventional semiconductor materials and air, in large planar semiconductors only 2-4 % of the photons emitted in the semiconductor are emitted in the escape cone of light in which the light can escape the semiconductor. Assuming no photon recycling, this results in EXE of 2-4 %. From the early 1990's, resonant cavity LEDs have been developed for improving extraction efficiency [22].

In resonant cavity LEDs, the optical mode distribution of the structure is engineered so that the number of guided optical modes is small and emission is stronger to the escape cone. Basically this is done by reducing at least one dimension of the device to the order of the wavelength and also by using distributed Bragg reflec-

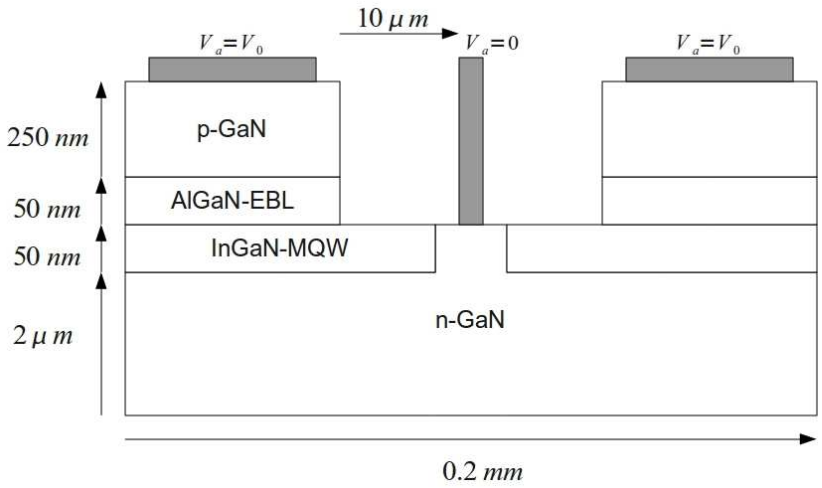


Figure 17: 2-dimensional cross-section of the basic unit of a transverse multi-quantum well junction LED. The actual LED is made by connecting multiple basic units together.

tors (DBRs). The spontaneous emission process becomes anisotropic so that more photons are emitted in the escape cone.

An accurate mode optimization of a resonant cavity LED structure requires numerical analysis based on electromagnetic theory and quantum optics. A few qualitative design rules can still be given for a resonant cavity LED design [33]:

- The reflectivity of the light-exit reflector should be much smaller than that of the back-reflector
- The thickness of the resonant cavity should be minimized
- The probability for self-absorption of photons should be small in the active region

In addition to resonant cavity LEDs, another efficient way of improving the light extraction is the device surface roughening. This has recently been done with GaN-based LEDs with laser lift-off and photoelectrochemical etching by T. Fujii *et al.* [55] and it is already in commercial use by Philips Lumileds. Further techniques of improving the extraction efficiency include e.g. shaping of the LED die and adding antireflective coatings.

# 6 Numerical methods

## 6.1 Finite Element Method (FEM)

Finite element method is one of the standard numerical methods for constructing approximate solutions for partial differential equation (PDE) systems in physics. It is based on discretizing the computational domain into small elements and using some simple element-specific basis functions to construct an approximate solution that minimizes the error.

In FEM, the computational domain is discretized into small elements like lines (1D), triangles (2D) or tetrahedrons (3D). Each element is further characterized by its nodal points $x_k$, one at each corner of the element and in case higher order basis functions are used, some at the edges or inside the element. The solution function $u$ is then approximated by a function $U$ which is constructed as a superposition of the basis functions $\varphi_i$:

$$U = \sum_{i=0}^{M} u_i \varphi_i, \tag{83}$$

where $u_i$ are real numbers and $M+1$ is the number of nodal points in the discretized problem.

Each basis function $\varphi_n$ is determined according to the following principles:

(i) at nodal point $x_n$, $\varphi_n(x_n) = 1$ and at all other nodal points $x_i \neq x_n$, $\varphi_n(x_i) = 0$

(ii) in the elements that are not next to the nodal point $x_n$, $\varphi_n(x) = 0$

(iii) in the elements next to the nodal point $x_n$, $\varphi_n$ is formed by any function, most often a linear or a higher order polynomial, that fulfils condition (i).

The formation of the element basis functions is demonstrated in Fig. 18, in which the use of piecewise linear basis functions in a 1-dimensional problem is sketched.

The idea of the FEM may be introduced with a simple example. In this thesis, we solve differential equations of the form

$$\nabla \cdot \xi(u, \mathbf{x}) = f(\mathbf{x}, u) \quad \text{in } \Omega, \tag{84}$$

where $\xi(u, \mathbf{x})$ is a vector consisting of the solution function $u(\mathbf{x})$ and its derivatives, $f(\mathbf{x}, u)$ is a load term and $\Omega$ is the computational domain (in this thesis a 2-dimensional space). In the elliptic problems solved in Chapter 7, $\xi$ contains only a gradient term so that

$$\xi(u, \mathbf{x}) = -a(\mathbf{x}, u)\nabla u(\mathbf{x}), \tag{85}$$

where $a(\mathbf{x}, u)$ is a coefficient function. Both $a(\mathbf{x}, u)$ and $f(\mathbf{x}, u)$ may have a highly nonlinear dependence of $u$. For notational simplicity, the dependences of $u$ and $\mathbf{x}$ are left out from the following equations.

To derive the variational form of the problem, Eq. (84) is multiplied by an arbitrary test function $v$ and integrated over the whole domain to get

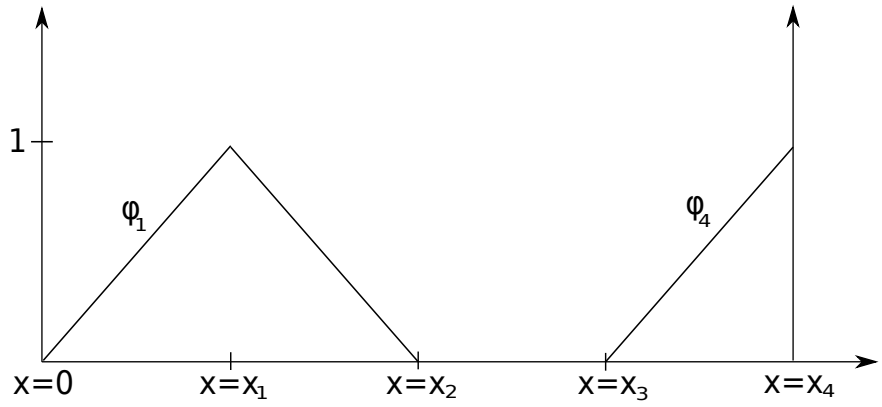


Figure 18: A 1-dimensional sketch of piecewise linear basis functions in the finite element method. Functions $\varphi_0$, $\varphi_2$ and $\varphi_3$ are not plotted in the figure. In this case the computational domain is $\Omega = (0, x_4)$ with the boundary $\Gamma = \{0, x_4\}$.

$$-\int_\Omega v\nabla \cdot (a\nabla u)d\Omega = \int_\Omega fv\, d\Omega. \tag{86}$$

By using Green's formula, Eq. (86) may be expressed as

$$\int_\Omega a(\nabla v)\cdot(\nabla u)d\Omega = \int_\Omega fv\, d\Omega + \int_\Gamma v(a\nabla u)\cdot \mathbf{n}\, d\Gamma, \tag{87}$$

where $\Gamma$ is the boundary of the domain. Eq. (87) gives the variational form of the problem that is solved using the FEM.

The boundary condition of the problem at a boundary $\Gamma_k$ can be of the form of the Dirichlet or Neumann boundary condition so that

$$\begin{cases} u = u_k & \text{on } \Gamma_k \quad \text{(Dirichlet)} \\ \mathbf{n}\cdot(a\nabla u) = g_k & \text{on } \Gamma_k \quad \text{(Neumann)}, \end{cases} \tag{88}$$

where $\mathbf{n}$ is the normal surface vector. In the case of a Neumann boundary condition, the last term in Eq. (87) reduces to $\int_\Gamma vg_k\, d\Gamma$ and the variational form is given by

$$\int_\Omega a(\nabla v)\cdot(\nabla u)d\Omega = \int_\Omega fv\, d\Omega + \int_\Gamma vg_k\, d\Gamma. \tag{89}$$

Homogeneous Dirichlet boundary conditions with $u_k = 0$ allow choosing the test function $v$ to have a zero value at the boundaries without loss of generality. Then the boundary term in Eq. (87) vanishes and the variational form is given by

$$\int_\Omega a(\nabla v)\cdot(\nabla u)d\Omega = \int_\Omega fv\, d\Omega. \tag{90}$$

Nonhomogeneous Dirichlet boundary conditions are slightly more complicated. They may be reduced back to the form (90) e.g. by choosing a sufficiently smooth

auxiliary function $u_{ext}$ that satisfies the nonhomogeneous Dirichlet boundary conditions and writing $u = \tilde{u} + u_{ext}$. Eq. (90) can then be rewritten as

$$\int_\Omega a(\nabla v) \cdot (\nabla \tilde{u}) d\Omega = \int_\Omega f v \, d\Omega - \int_\Omega a(\nabla v) \cdot (\nabla u_{ext}) \, d\Omega. \tag{91}$$

In the finite element method, the variational form is discretized by approximating $u$ and $v$ by functions $U$ and $V$ constructed from the basis functions. In the case of the Neumann boundary conditions, $U$ and $V$ are substituted into Eq. (89) which after simplification gives

$$\sum_{i=0}^{M} \sum_{j=0}^{M} u_i v_j \int_\Omega a(\nabla \varphi_i) \cdot (\nabla \varphi_j) \, d\Omega =$$

$$\sum_{j=0}^{M} v_j \int_\Omega f \varphi_j \, d\Omega + \sum_{j=0}^{M} v_j \int_\Gamma \varphi_j g_k \, d\Gamma. \tag{92}$$

Eq. (92) must hold for arbitrary values of $v_j$. It is sufficient for the equation to hold separately for each $j$ since if the equation holds for all the basis functions, it holds for all their linear combinations. Hence the equation may be written as

$$\sum_{i=0}^{M} u_i \int_\Omega a(\nabla \varphi_i) \cdot (\nabla \varphi_j) \, d\Omega = \int_\Omega f \varphi_j \, d\Omega + \int_\Gamma \varphi_j g_k \, d\Gamma, \tag{93}$$

for all $j \in [0, M]$. Eq. (93) may be expressed as a matrix equation:

$$\mathbf{A}\mathbf{u} = \mathbf{f}, \tag{94}$$

where

$$A_{i,j} = \int_\Omega a(\nabla \varphi_i) \cdot (\nabla \varphi_j) \, d\Omega, \tag{95}$$

$$f_j = \int_\Omega f \varphi_j \, d\Omega + \int_\Gamma \varphi_j g_k \, d\Gamma \tag{96}$$

and $\mathbf{u}$ is a vector containing the values of $u_i$. In the case of homogeneous Dirichlet boundary conditions with the boundary values set to zero, $\mathbf{f}$ is given by

$$f_j = \int_\Omega f \varphi_j \, d\Omega \tag{97}$$

and in the case of nonhomogeneous Dirichlet boundary conditions, $\mathbf{A}$ and $\mathbf{f}$ are given by

$$A_{i,j} = \int_\Omega a(\nabla \varphi_i) \cdot (\nabla \varphi_j) \, d\Omega \tag{98}$$

and

$$f_j = \int_\Omega f\varphi_j \, d\Omega - \int_\Omega a(\nabla u_{ext}) \cdot (\nabla \varphi_j) \, d\Omega \tag{99}$$

and the final approximate solution is given by $U + u_{ext}$ [56, 57].

If the initial differential equation is linear, calculating the values $u_i$ requires only multiplying Eq. (94) by the inverse of $\mathbf{A}$. If the system is nonlinear, Eq. (94) must be solved with an iterative procedure. The residual for the equation can be defined as

$$\mathbf{r}(\mathbf{u}) = \mathbf{A}(\mathbf{u})\mathbf{u} - \mathbf{f}(\mathbf{u}) \tag{100}$$

and the vector $\mathbf{u}$ must be solved so that it minimizes the residual. A standard method to do this is to apply the Newton-Raphson method with an initial guess $\mathbf{u}_0$:

$$\mathbf{u}_{r+1} = \mathbf{u}_r - \mathbf{T}^{-1}(\mathbf{u}_r)\mathbf{r}(\mathbf{u}_r), \tag{101}$$

where $\mathbf{T}(\mathbf{u}_r)$ is the tangent matrix:

$$[\mathbf{T}_{i,j}] = \frac{\partial r_i}{\partial u_{r,j}}. \tag{102}$$

The iteration of Eq. (101) is continued until the residual reaches a sufficiently small value or until $\mathbf{u}_r$ does not change notably between successive steps. In some cases it may be useful to add an additional damping factor to make the iteration more stable, so that

$$\mathbf{u}_{r+1} = \mathbf{u}_r - d_r\mathbf{T}^{-1}(\mathbf{u}_r)\mathbf{r}(\mathbf{u}_r), \tag{103}$$

where small values of $d_r$ decrease the change of $\mathbf{u}_r$ between successive steps.

The solution produced by FEM is the best for the chosen function basis and the error decreases rapidly by reducing the element size. In 2D, best stability is achieved by using triangles or quadrilaterals with approximately equal side lengths.

### 6.1.1 Semiconductor equations with FEM

The variational forms for Eqs. (33) are derived in the same way as in the previous section. Poisson's equation in the variational form is given by

$$\int_\Omega \varepsilon\nabla\phi \cdot \nabla v \, d\Omega = \int_\Omega \left(fv + \nabla v \cdot \mathbf{P}_{tot}\right) \, d\Omega + \int_\Gamma v \left(\varepsilon\nabla\phi - \mathbf{P}_{tot}\right) \cdot \mathbf{n} \, d\Gamma, \tag{104}$$

where the source term is $f(\phi, \phi_n, \phi_p) = q\left(p - n + N_d^+ - N_a^-\right)$. The variational forms for the current equations are given by

$$\int_\Omega \mu_n n(\nabla v) \cdot (\nabla \phi_n) \, d\Omega = \int_\Omega Rv \, d\Omega + \int_\Gamma v \left(\mu_n n \nabla \phi_n\right) \cdot \mathbf{n} \, d\Gamma \tag{105}$$

for the electron current and

$$\int_\Omega \mu_p p(\nabla v)\cdot(\nabla\phi_p)\,d\Omega = -\int_\Omega Rv\,d\Omega + \int_\Gamma v\,(\mu_p p\nabla\phi_p)\cdot\mathbf{n}\,d\Gamma \tag{106}$$

for the hole current. Note that all the boundary terms vanish when insulator boundaries are assumed.

## 6.2 Scaling of the equations

In the structures modeled in this thesis, the dimensions in the orthogonal directions differ from each other by a factor of approximately $10^4$. This results in an unnecessarily dense mesh in the longer dimension. The problems introduced by different dimensions of the computational domain may be partly avoided by scaling the equations presented in Section 2.3.

In a 2-dimensional space, the equations can be written in unitless dimensions $x' = x/L_x$ and $y' = y/L_y$, where $L_x$ and $L_y$ are scaling factors in the two orthogonal directions. The differential operators are then given by

$$\nabla = \mathbf{u}_x\frac{1}{L_x}\frac{d}{dx'} + \mathbf{u}_y\frac{1}{L_y}\frac{d}{dy'} \tag{107}$$

$$\nabla^2 = \frac{1}{L_x^2}\frac{d^2}{dx'^2} + \frac{1}{L_y^2}\frac{d^2}{dy'^2}. \tag{108}$$

Choosing the $y$ axis to be the same as the direction of internal polarizations so that $\mathbf{u}_x\cdot\mathbf{P}_{int} = 0$, Poisson's equation in a scaled form is given by

$$-\varepsilon\left(\frac{1}{L_x^2}\frac{d^2}{dx'^2} + \frac{1}{L_y^2}\frac{d^2}{dy'^2}\right)\phi + \left(\mathbf{u}_x\frac{1}{L_x}\frac{d}{dx'} + \mathbf{u}_y\frac{1}{L_y}\frac{d}{dy'}\right)\cdot\mathbf{P}_{int} = q(p - n + N_d - N_a)$$

$$\Rightarrow \nabla'\cdot\left[-\varepsilon\left(\mathbf{u}_x\frac{1}{L_x^2}\frac{d}{dx'} + \mathbf{u}_y\frac{1}{L_y^2}\frac{d}{dy'}\right)\phi + \frac{1}{L_y}\mathbf{P}_{int,y}\right] = q(p - n + N_d - N_a), \tag{109}$$

where $\nabla' = \mathbf{u}_x\frac{d}{dx'} + \mathbf{u}_y\frac{d}{dy'}$. Multiplying Eq. (109) by $L_y$ makes dealing with internal boundaries easier and results in

$$-\nabla'\cdot\left[-\varepsilon\left(\mathbf{u}_x\frac{L_y}{L_x^2}\frac{d}{dx'} + \mathbf{u}_y\frac{1}{L_y}\frac{d}{dy'}\right)\phi + \mathbf{P}_{int,y}\right] = L_y q(p - n + N_d - N_a). \tag{110}$$

The drift-diffusion equations in scaled form multiplied by $L_y$ are correspondingly given by

$$-\nabla'\cdot\left[\mu_n n\left(\mathbf{u}_x\frac{L_y}{L_x^2}\frac{d}{dx'} + \mathbf{u}_y\frac{1}{L_y}\frac{d}{dy'}\right)\phi_n\right] = L_y R \tag{111}$$

for the electron current and

$$-\nabla' \cdot \left[ \mu_p p \left( \mathbf{u}_x \frac{L_y}{L_x^2} \frac{d}{dx'} + \mathbf{u}_y \frac{1}{L_y} \frac{d}{dy'} \right) \phi_p \right] = -L_y R \tag{112}$$

for the hole current. The computational domain dimensions may now be transformed by choosing values for $L_x$ and $L_y$ and solving the scaled Eqs. (110), (111) and (112).

Scaling affects the implementation of the Neumann boundary conditions. The Neumann conditions must be applied as in Eqs. (34) and (35), i.e. $\mathbf{n} \cdot \xi = 0$ for insulating boundaries and $\mathbf{n} \cdot \xi_1 = \mathbf{n} \cdot \xi_2$ for interior boundaries, where $\xi$ is the field term of the equations so that

$$\begin{cases} \xi_P = -\varepsilon \nabla \phi + \mathbf{P}_{int} \\ \xi_n = \mu_n n \nabla \phi_n \\ \xi_p = \mu_p p \nabla \phi_p \end{cases} \tag{113}$$

and subindices 1 and 2 refer to the materials delimited by the internal boundary. In the models of this thesis, every boundary is parallel to either the $x$ or the $y$ direction. The boundary terms for the scaled equations are given by

$$\begin{cases} \mathbf{n} \cdot \xi_{P,\text{scaled}} = \mathbf{n} \cdot \left[ -\varepsilon \left( \mathbf{u}_x \frac{L_y}{L_x^2} \frac{d}{dx'} + \mathbf{u}_y \frac{1}{L_y} \frac{d}{dy'} \right) \phi + \mathbf{P}_{int,y} \right] \\ \mathbf{n} \cdot \xi_{n,\text{scaled}} = \mathbf{n} \cdot \left[ \mu_n n \left( \mathbf{u}_x \frac{L_y}{L_x^2} \frac{d}{dx'} + \mathbf{u}_y \frac{1}{L_y} \frac{d}{dy'} \right) \phi_n \right] \\ \mathbf{n} \cdot \xi_{p,\text{scaled}} = \mathbf{n} \cdot \left[ \mu_p p \left( \mathbf{u}_x \frac{L_y}{L_x^2} \frac{d}{dx'} + \mathbf{u}_y \frac{1}{L_y} \frac{d}{dy'} \right) \phi_p \right]. \end{cases} \tag{114}$$

Now if $\mathbf{n} = \mathbf{u}_y$,

$$\begin{cases} \mathbf{n} \cdot \xi_{P,\text{scaled}} = -\varepsilon \frac{1}{L_y} \frac{d}{dy'} \phi + P_{int,y} = \mathbf{n} \cdot \xi_P \\ \mathbf{n} \cdot \xi_{n,\text{scaled}} = \mu_n n \frac{1}{L_y} \frac{d}{dy'} \phi_n = \mathbf{n} \cdot \xi_n \\ \mathbf{n} \cdot \xi_{p,\text{scaled}} = \mu_p p \frac{1}{L_y} \frac{d}{dy'} \phi_p = \mathbf{n} \cdot \xi_p, \end{cases} \tag{115}$$

which are the same as the boundary conditions in a non-scaled form. This indicates that all the boundary conditions in the chosen $y$ direction are preserved. If $\mathbf{n} = \mathbf{u}_x$, we have

$$\begin{cases} \mathbf{n} \cdot \xi_{P,\text{scaled}} = -\varepsilon \frac{L_y}{L_x^2} \frac{d}{dx'} \phi = \frac{L_y}{L_x} (\mathbf{n} \cdot \xi_P) \\ \mathbf{n} \cdot \xi_{n,\text{scaled}} = \mu_n n \frac{L_y}{L_x^2} \frac{d}{dx'} \phi_n = \frac{L_y}{L_x} (\mathbf{n} \cdot \xi_n) \\ \mathbf{n} \cdot \xi_{p,\text{scaled}} = \mu_p p \frac{L_y}{L_x^2} \frac{d}{dx'} \phi_p = \frac{L_y}{L_x} (\mathbf{n} \cdot \xi_p). \end{cases} \tag{116}$$

It can be seen that the insulating boundary conditions ($\mathbf{n} \cdot \xi = 0$) are preserved also in the chosen $x$ direction. On the other hand, the interior boundary conditions are scaled in this direction, which must be properly handled when performing numerical simulations. In this thesis, there are some internal boundaries in the $x$ direction but as the scaling factors across these boundaries are kept constant, no special internal boundary conditions need to be used.

# 7 Numerical results & discussion

In this Chapter the numerical results obtained for the 2-dimensional TFFC (Fig. 16) and TMJ (Fig. 17) LED structures presented in Chapter 5 are studied in more detail. The key quantities that affect the performance and the efficiency of LEDs include e.g. the electrostatic potential in the current channel, the changes in the quasi-Fermi potentials and the quasi-Fermi level separation in the active region. The presented results focus on studying the effect these performance parameters have on the optical power, the spatial emission distribution and the key efficiency figures.

A more detailed structure of the active MQW region used in the simulations is shown in Fig. 19. Figure also shows eight paths that will be used in presenting the numerical results. The width of the simulated structures is 100 $\mu$m, which corresponds to a separation of 200 $\mu$m between the n-type contacts. The active region in both simulated structures consists of a 10 nm thick blue-emitting InGaN QW, a 10 nm thick GaN barrier layer and a 10 nm thick green-emitting InGaN QW. All the QWs in the active region are undoped. The structure with two QWs emitting green and blue light is chosen to study the ability of these structures to emit two different wavelengths simultaneously. This property could be used in producing white light as noted in Chapter 3.

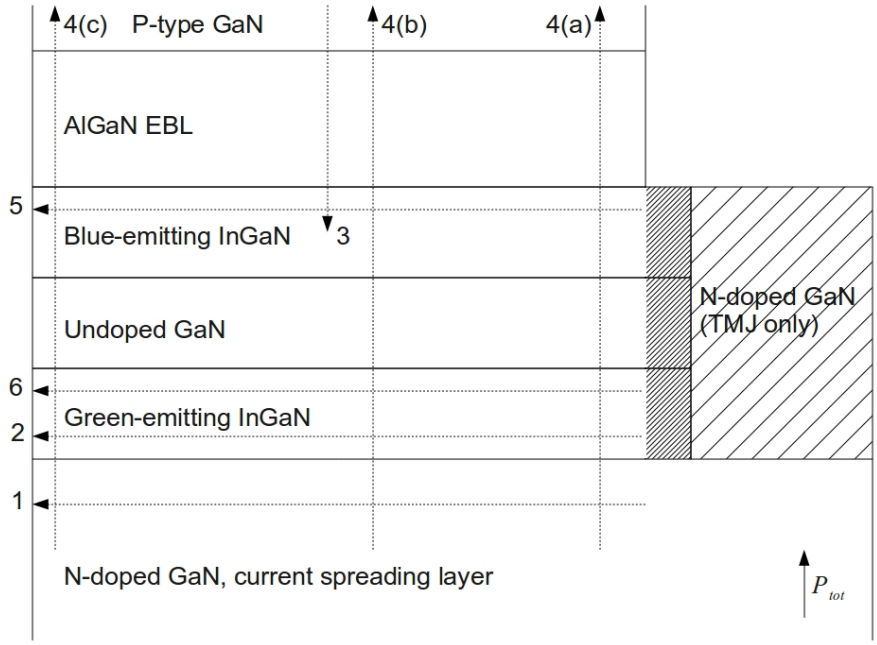


Figure 19: Schematic structure of the active material layer and its surroundings used in the simulation of both LED structures. The shaded area is present only in the TMJ structure and enables direct current injection to the QWs. The arrows describe the paths for which various physical properties are calculated below, and reference to the arrows is made frequently in the following sections. The direction for $\mathbf{P}_{tot}$ is also marked in the figure. Note that the material layer thicknesses are not scaled correctly in the figure.

Material parameters, layer thicknesses and doping densities used in the calculations are shown in Table 6. For nitrides the radiative recombination parameter $B$ is slightly smaller and the SRH recombination parameter $A$ is slightly larger than the typical values for the conventional III-V semiconductors. Both values are taken from the nitride literature. The default temperature used in the calculations is 350 K but in Section 7.5, effects of an elevated temperature of 400 K are briefly discussed for comparison. Note that ideal extraction is assumed when calculating optical powers and efficiencies.

Table 6: Material parameter values, layer thicknesses and doping densities used in the calculations. Identical recombination parameters are used for all material compositions. The abbreviation CSL stands for the current spreading layer. Effective densities of states are given for the temperature of 350 K. The values of the parameters are obtained from Refs. [8, 11, 14, 17, 40].

| Property | GaN | $Ga_{0.83}In_{0.17}N$ | $Ga_{0.75}In_{0.25}N$ | $Ga_{0.80}Al_{0.20}N$ | Unit |
|---|---|---|---|---|---|
| $\varepsilon$ | 8.90 | 9.99 | 10.50 | 8.95 | $\varepsilon_0$ |
| $a$ | 3.19 | 3.25 | 3.28 | 3.18 | Å |
| $E_g$ | 3.44 | 2.63 | 2.31 | 3.83 | eV |
| $\mu_n$ | 0.100 | 0.137 | 0.154 | 0.088 | $m^2/Vs$ |
| $\mu_p$ | 0.007 | 0.006 | 0.006 | 0.006 | $m^2/Vs$ |
| $m_e^*$ | 0.200 | 0.185 | 0.178 | 0.240 | $m$ |
| $m_h^*$ | 1.401 | 1.440 | 1.459 | 1.828 | $m$ |
| $N_c$ | $2.83 \cdot 10^{24}$ | $2.51 \cdot 10^{24}$ | $2.36 \cdot 10^{24}$ | $3.71 \cdot 10^{24}$ | $1/m^3$ |
| $N_v$ | $5.23 \cdot 10^{25}$ | $5.45 \cdot 10^{25}$ | $5.56 \cdot 10^{25}$ | $7.80 \cdot 10^{25}$ | $1/m^3$ |
| $P_{tot}$ | -0.0339 | -0.0081 | 0.0060 | -0.0472 | $C/m^2$ |
| $P_{sp}$ | -0.0339 | -0.0298 | -0.0287 | -0.0420 | $C/m^2$ |
| $P_{pz}$ | 0 | 0.0217 | 0.0347 | -0.0052 | $C/m^2$ |
| Role | n-CSL/barrier/p-CSL | Blue QW | Green QW | p-EBL | |
| Thickness | 2000/10/250 | 10 | 10 | 50 | nm |
| Doping | $10^{24}/0/10^{24}$ | 0 | 0 | $7.5 \cdot 10^{23}$ | $1/m^3$ |
| $A$ | | $10^7$ | | | 1/s |
| $B$ | | $4 \cdot 10^{-17}$ | | | $m^3/s$ |
| $C$ | | $10^{-42}$ | | | $m^6s$ |

## 7.1 Current-voltage relation

The applied voltage as a function of the average current density is shown in Fig. 20. The LEDs start to significantly conduct current when the bias voltage is above approximately 3 V. At lower voltages the output power is too low for using the devices as LEDs. Close to 3 V the current density grows rapidly as a function of the voltage but as the bias voltage increases, the increase in the current density slows down due to the growing role of resistive losses and Ohm's law. In both simulated LEDs the current starts to saturate above a current density value of 100 $A/cm^2$.

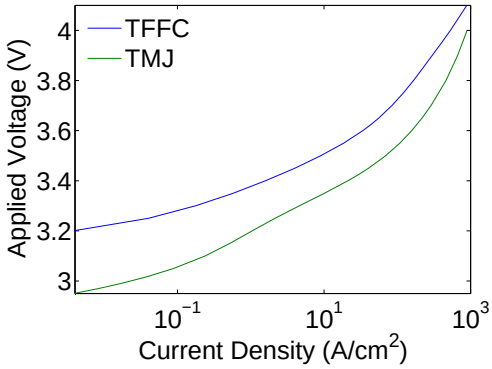


Figure 20: The bias voltage as a function of the average current density through the LED.

Note that the TMJ LED switches on at a significantly lower bias voltage than the TFFC LED. This effect presumably originates from the current component created by the horizontal injection to the QWs in the TMJ LED, effectively decreasing potential changes between the QWs and barriers.

## 7.2 Resistive losses

The changes in the electrostatic potential and the quasi-Fermi potential along the current path significantly affect the efficiency and the spatial homogeneity of the emitted light. In the lateral horizontal direction the changes are mainly caused by resistive loss mechanisms which strongly reduce the emitted optical power at large current densities when moving away from the n-type contact. In the vertical direction normal to the QW interfaces there are, on the other hand, large changes in the quasi-Fermi potentials caused by the current blocking of the potential barriers.

Fig. 21 shows the change in the electrostatic potential and the quasi-Fermi potentials for electrons and holes in the TFFC and TMJ structures between the endpoints of Paths 1, 2 and 3 in Fig. 19, respectively. The lateral change of $\phi_n$ in the current spreading layer (not shown) is approximately equal to the change of $\phi$ (the blue curve in Fig. 21). The most notable difference of the structures is that in the TMJ there is no visible difference between $\Delta\phi_n$ and $\Delta\phi$ whereas in the TFFC, $\Delta\phi$ is clearly larger than $\Delta\phi_n$ at large current densities.

In the TFFC LED, the lateral drop in $\phi_n$ is $k_BT$ at a current density of approximately 44 A/cm$^2$, and in the TMJ LED the corresponding current density value is approximately 33 A/cm$^2$. While this potential drop does not have a large effect on the power efficiency, at this operating point the output power at the edges of the active region has already been clearly reduced. The potential drop starts to increase very strongly when the current density is greater than 100 A/cm$^2$, which corresponds to the onset of the ohmic losses in Fig. 20.

The change in the quasi-Fermi potential for holes ($\Delta\phi_p$) is much larger in the TFFC LED than in the TMJ LED at low current densities. Also, in the TMJ structure the change increases with the current density in contrast to the TFFC

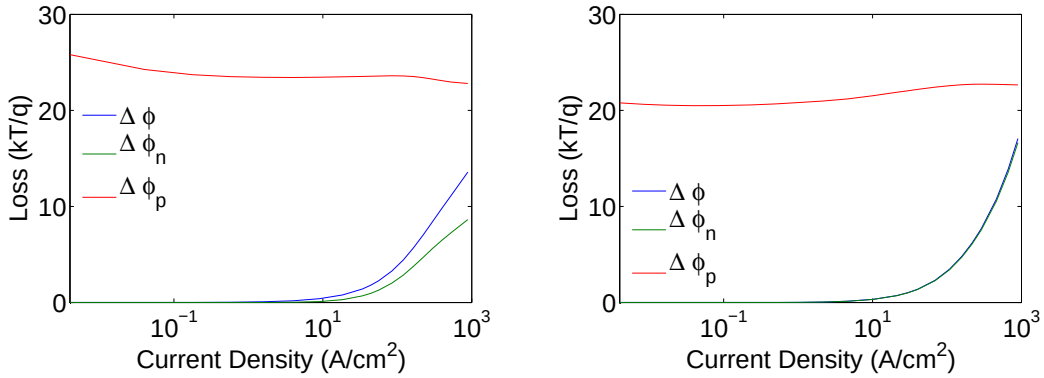


(a) TFFC LED. (b) TMJ LED.

Figure 21: Lateral change in the electrostatic potential ($\Delta\phi$) and the electron quasi-Fermi potential ($\Delta\phi_n$), and vertical change in the hole quasi-Fermi potential ($\Delta\phi_p$) between the endpoints of Paths 1, 2 and 3 of Fig. 19. The homogeneity of the emission is mainly affected by the lateral change of the electron quasi-Fermi level along Path 2.

structure. This is a somewhat surprising result and presumably has its origins in the direct horizontal carrier injection component in the TMJ LED.

The changes in the quasi-Fermi levels in the vertical direction occur close to the edges of the quantum wells and they are mainly caused by potential barriers around the interfaces. To demonstrate the changes, the band diagrams through the active region of the LEDs close to and far away from the n-type contacts along Paths 4(a) and 4(c) are shown for the TFFC LED and for the TMJ LED in Figs. 22 and 23, respectively. The current density in the figures is 166 A/cm$^2$ for the TFFC and 176 A/cm$^2$ for the TMJ structure. Note that QWs are approximated as bulk structures when calculating the band diagram.

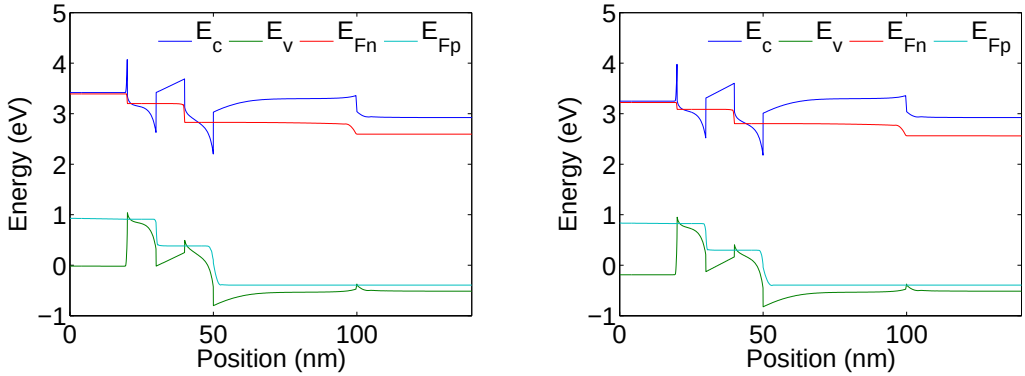


(a) Near the n-type contact. (b) Near the left-side end.

Figure 22: The band diagram of the TFFC LED (a) along Path 4(a) of Fig. 19 near the n-type contact and (b) along Path 4(c) of Fig. 19 near the left-side end of the structure. The current density is 166 A/cm$^2$ and the bias voltage is 3.80 V.

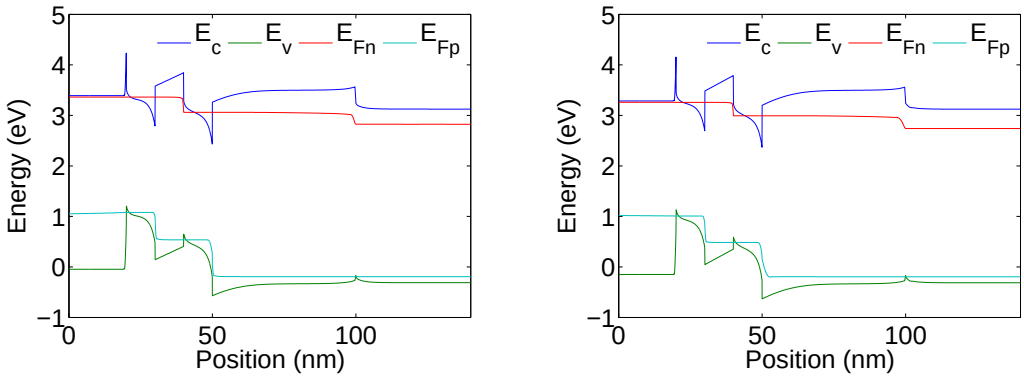


(a) Near the n-type contact.

(b) Near the left-side end.

Figure 23: The band diagram of the TMJ LED (a) along Path 4(a) of Fig. 19 near the n-type contact and (b) along Path 4(c) of Fig. 19 near the left-side end of the structure. The current density is 176 A/cm$^2$ and the bias voltage is 3.60 V.

In both LEDs, relatively large vertical changes in the quasi-Fermi levels can be seen at the edges of the QWs except for the interface between the green well and the n-type current spreading layer in the TMJ structure where the change is very small. Moreover, on a closer observation of Fig. 22 it can be seen that the change in $E_{Fn}$ in the TFFC LED at the edge of the green QW decreases further away from the n-type contact. This decrease explains the difference between $\Delta\phi$ and $\Delta\phi_n$ seen in Fig. 21(a). The band diagrams also give an explanation for the distinct current-voltage characteristics of the LEDs. By studying the band diagrams, the total drop in $E_{Fn}$ over the active region is found to differ by approximately 0.2 eV between the two structures. Based on the simulations, the difference in the threshold voltages between the structures is approximately equal to this value. Therefore the threshold voltage difference presumably originates from the more efficient injection of electrons to the QWs in the TMJ structure.

The effects of the internal polarization fields are also clearly visible in the band diagrams of Figs. 22 and 23, as the bands in the QWs are strongly bent. In these models the polarization-induced surface charges contribute to a significant Auger recombination rate in the QWs, decreasing the IQE. To demonstrate this effect, the predicted recombination rate in the TFFC LED along Path 4(b) is shown in Fig. 24. The recombination profile of the TMJ LED (not shown) is qualitatively similar. It is seen that the model predicts a significant Auger recombination rate near the edges of the active QWs. This is in part caused by the internal polarization fields and their changes across the internal boundaries, and it causes the internal quantum efficiencies of the LEDs to remain relatively low.

The lateral potential drop follows quite well the treatment presented in Section 2.4.1. In Section 2.4.1, the optical intensity corresponding to a potential drop of $k_BT/q$ over a 100 $\mu$m wide current spreading layer was calculated to be 0.6 W/mm$^2$. The numerical models predict an optical intensity of approximately 0.66 W/mm$^2$ for the TFFC structure and 0.53 W/mm$^2$ for the TMJ structure with the same quasi-Fermi potential drop.

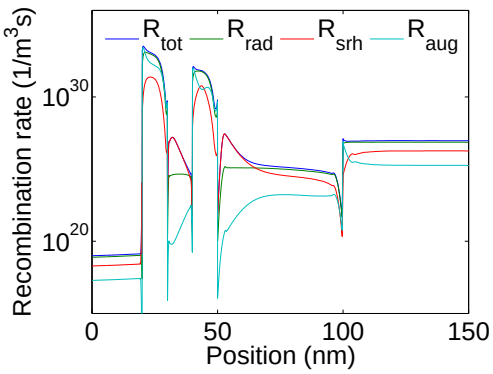


Figure 24: Total recombination rate and all the different recombination mechanisms along Path 4(b) of Fig. 19 in the center of the TFFC LED, starting in the n-type GaN layer and ending in the p-type GaN layer. The current density is approximately 166 A/cm$^2$ and the voltage is 3.80 V.

## 7.3 Device performance and color balance

The overall power efficiency calculated for the simulated structures is shown in Fig. 25(a). The overall efficiency is slightly higher in the TMJ LED than in the TFFC LED. According to the numerical results, the main reason for this is the smaller threshold voltage than in the TFFC structure. Due to the smaller threshold voltage in the TMJ LED, less electrical energy is required to produce a similar optical power.

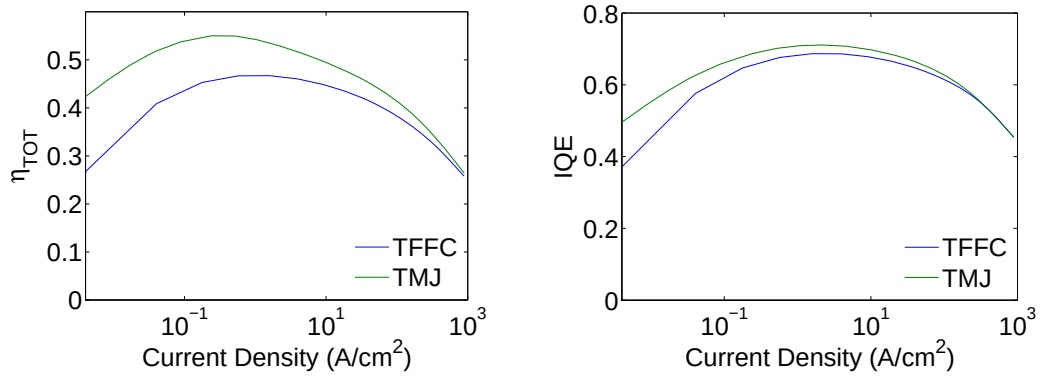


(a) Overall efficiency.

(b) Internal quantum efficiency.

Figure 25: Overall efficiency and internal quantum efficiency as a function of the current density. The overall IQE is calculated as a ratio of the total radiative recombination to the total recombination, both integrated over the whole active region.

The overall internal quantum efficiency in the active region is shown in Fig. 25(b). In both structures it is smaller than the theoretical maximum of 0.87 given by Eq. (65), originating from the strong Auger recombination at the edges of the active region. Moreover, it can be seen that the IQE is slightly higher in the TMJ

LED at low current densities. The injection efficiencies of both LEDs are found to be almost ideal in the simulations.

The quasi-Fermi level separation and the average optical intensity emitted by the quantum wells are the key parameters determining the proportions of green and blue light emitted by the wells. These quantities are shown in Fig. 26. Based on the chromaticity analysis presented in Section 3.5 and the wavelengths emitted by the simulated QWs, approximately 60 % of the total light intensity should be blue in order to give chromaticity coordinates corresponding to nearly white light. However, in this thesis the main focus is more in the general feasibility of mixing green and blue emission than in finding the optimal conditions for producing white light.

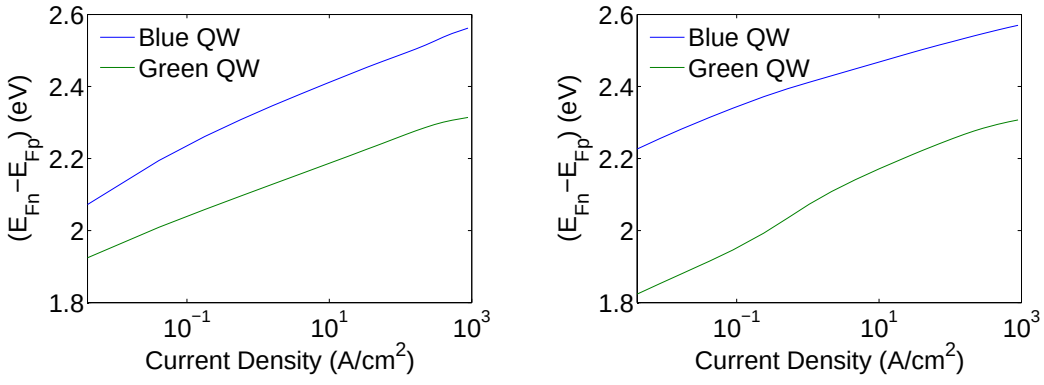


(a) TFFC LED. (b) TMJ LED.

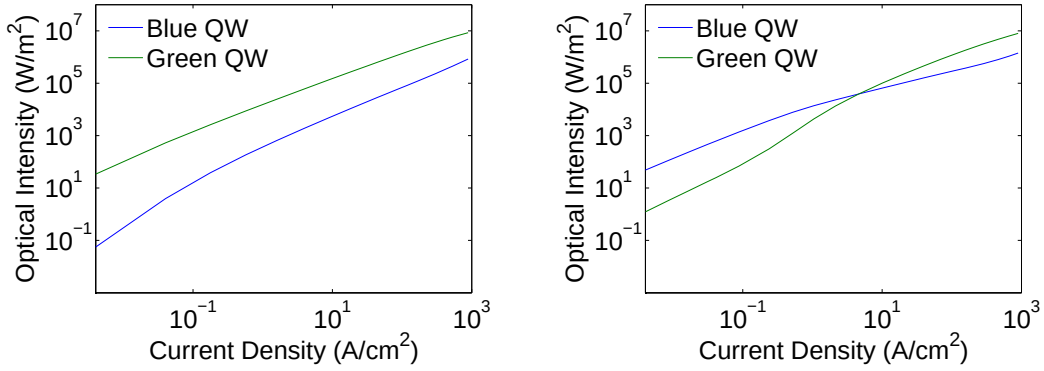


(c) TFFC LED. (d) TMJ LED.

Figure 26: (a), (b) Average separation between the quasi-Fermi levels in the quantum wells and (c), (d) average optical intensity in the quantum wells. The energy gaps of the blue and green wells are 2.63 eV and 2.31 eV, respectively.

At current densities higher than approximately 5 A/cm$^2$, the emission from the green QW is stronger in both structures. At lower current densities the emission distribution in the TMJ structure is fundamentally different as the emission from the blue quantum well dominates over the emission from the green well. The numerical results and the band diagrams in particular suggest that at low current densities, the location of the n-type contact next to the QWs enables efficient electron injection

to both wells in the TMJ structure. However, hole injection is more efficient to the blue well located closer to the p-type contact. At larger current densities the role of direct electron injection decreases and the emission from the green QW becomes stronger than the emission from the blue QW.

The intensities of the blue and green light emitted by the two quantum wells in the TMJ LED are approximately equal when the current density is slightly less than 10 A/cm$^2$, as seen in Fig. 26(d). However, this current density is somewhat too low for emitting useful amounts of light. Making the QWs thinner and increasing their number could make it easier to produce equivalent amounts of blue and green light with higher current density values in both LEDs.

## 7.4 Current spreading in narrow structures

The maximum practical distance between the n-type contacts is limited by the lateral resistive losses. For example, if the distance between the two n-type contacts is 1 mm, the quasi-Fermi potential drop in the TFFC LED active material layer is more than $2k_BT/q$ with a current density of 2 A/cm$^2$ in 350 K, and the intensity at the center of the LED is reduced by approximately a factor of $e^2$ with respect to the intensity at the contact. Increasing the current further increases the contrast. To demonstrate this, Fig. 27 shows the rate of radiative recombination in the simulated structures along Paths 5 and 6 with high current densities. It can be seen that the lateral resistive losses strongly reduce the recombination rate far from the n-type contact.

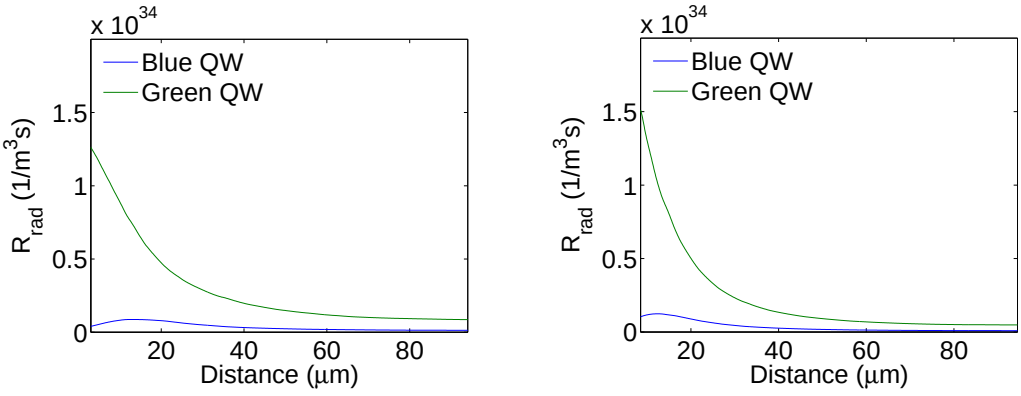


(a) TFFC LED. (b) TMJ LED.

Figure 27: Rate of radiative recombination along Paths 5 and 6 of Fig. 19 in the centers of the quantum wells at high current densities. The current density and bias voltage are 886 A/cm$^2$ and 4.10 V in the TFFC LED and 896 A/cm$^2$ and 4.00 V in the TMJ LED.

Reducing the separation between the n-type contacts allows reaching higher current densities without significant lateral potential drops. However, reducing the size eventually increases other losses like the absorption by the contacts and the surface recombination. As a compromise between the potential drops, increased losses and

fabrication challenges, selected numerical results are calculated for structures with a separation of 20 $\mu$m between the n-type contacts. Note that upon reducing the n-type contact separation to 20 $\mu$m, the horizontal separation between the n-type contact and the EBL is also reduced to be only 5 $\mu$m in the TMJ LED (see Fig. 17 in Chapter 5).

Fig. 28 shows the change in the electrostatic potential and the quasi-Fermi potentials for electrons and holes in the narrow TFFC and TMJ structures between the endpoints of Paths 1, 2 and 3 of Fig. 19, respectively. It is seen that the lateral potential drop through the current spreading layer is small even with current densities close to 1000 A/cm$^2$. This is the evident advantage of the narrow structures, as the light is homogeneously emitted by the whole active region with all practically usable current values.

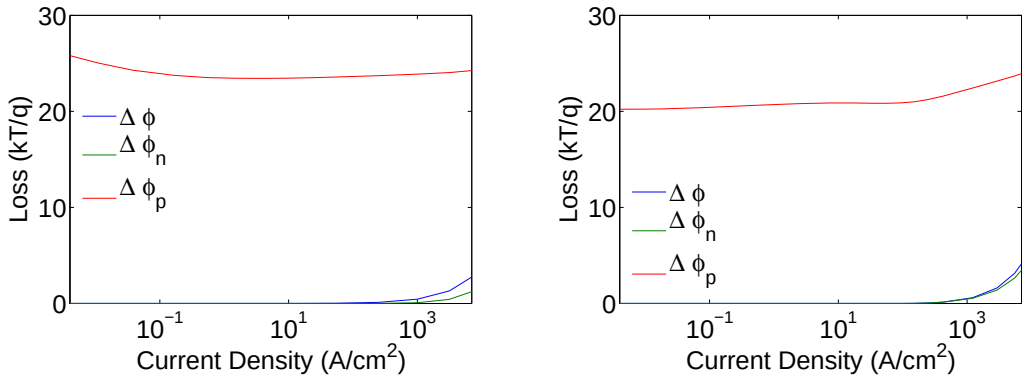


(a) TFFC LED. (b) TMJ LED.

Figure 28: Lateral drop in the electrostatic potential ($\Delta\phi$), lateral drop in the electron quasi-Fermi potential ($\Delta\phi_n$) and vertical drop in the hole quasi-Fermi potential ($\Delta\phi_p$) for narrow structures between the endpoints of Paths 1, 2 and 3 of Fig. 19, respectively. The n-type contact separation is 20 $\mu$m in these figures.

The average emitted optical intensity of both LEDs is shown in Fig. 29. It can be seen that the optical intensity of the wells of the TFFC LED is not significantly affected by reducing the current spreading layer width. Conversely, in the narrow TMJ LED the blue QW is found to emit significantly more light than the green QW with current densities smaller than approximately 500 A/cm$^2$. Reducing the width of the TMJ structure therefore facilitates the direct current injection to the blue QW over a large current density range.

The overall efficiency of both narrow LEDs is shown in Fig. 30. The overall efficiency of the TFFC LED has not changed essentially from the values presented in Section 7.3, whereas the overall efficiency of the TMJ LED has slightly improved. This is caused by the increased contribution of the direct current component, leading to smaller resistive power losses.

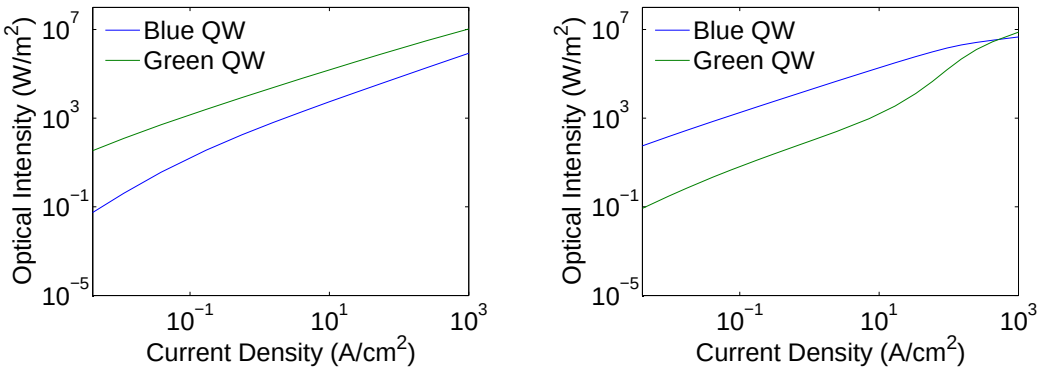


(a) TFFC LED. (b) TMJ LED.

Figure 29: Average optical intensity in the quantum wells, when the n-type contact separation is 20 $\mu$m.

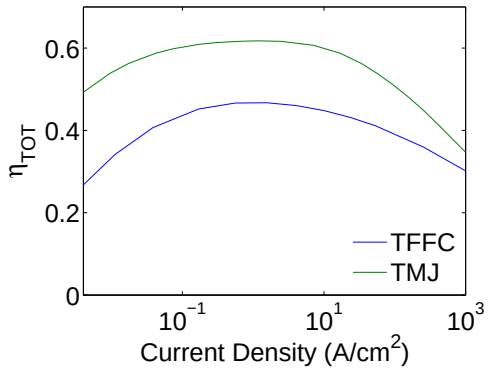


Figure 30: Overall efficiency as a function of the average current density, when the n-type contact separation is 20 $\mu$m.

## 7.5 Effects of a higher temperature

Selected simulation results calculated for the temperature 400 K are shown in this section for comparison. In Fig. 31, the current-voltage relation is shown. It can be seen that the threshold voltage is decreased by approximately 0.1-0.2 V in both structures compared to 350 K, due to the higher thermal energy $k_BT$ and the resulting higher carrier density values.

Average optical intensity in both LEDs is shown in Fig. 32. The proportions of blue and green light in the TMJ LED are better balanced in the low current density range. It seems that the higher temperature facilitates the transport of carriers over the potential barriers, effectively equalizing the carrier densities in both QWs at low current density values.

The overall efficiency of the LEDs is shown in Fig. 33. By comparing with Fig. 25(a) it can be seen that the efficiencies remain approximately equal as the temperature is raised from 350 K to 400 K. Note that the recombination parameters do not depend on the temperature in the simulations.

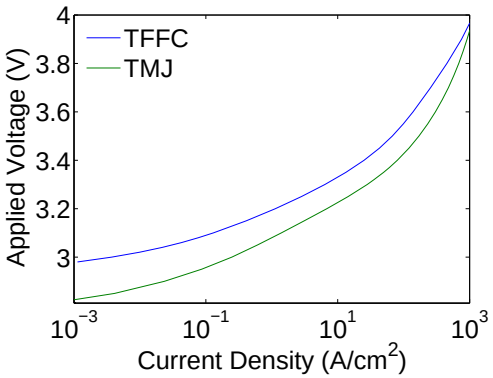


Figure 31: Applied voltage as a function of the average current density in the p-type GaN layer at 400 K.

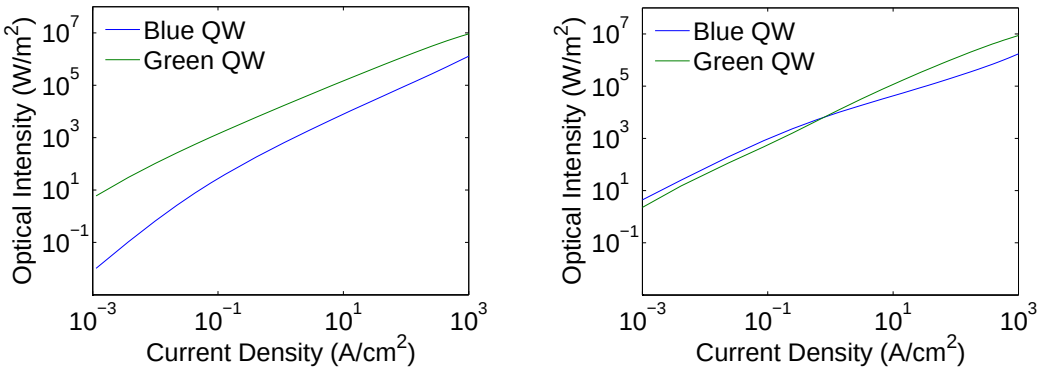


(a) TFFC LED.

(b) TMJ LED.

Figure 32: Average optical intensity in the quantum wells at 400 K.

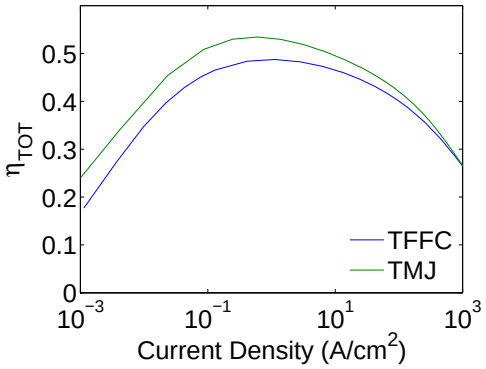


Figure 33: Overall efficiency as a function of the current density at 400 K.

## 7.6 Overview of the numerical results

Table 7 gives an overview of the key performance parameters of the LED structures at 350 and 400 K. The values calculated for the TFFC LED are generally in a good agreement with the published experimental data [49] of Table 4. The results for the TMJ LED show a slightly better quantum efficiency than the TFFC LED due to the operation closer to the optimal carrier densities. The overall efficiency in the TMJ LED is also found to be slightly higher than in the TFFC LED due to smaller bias voltages and hence smaller resistive losses. The calculated injection efficiency is close to unity in both structures.

Table 7: Selected performance parameters of the simulated structures assuming a total emitting area of 1 mm$^2$.

350 K

| TFFC | | | | TMJ | | | |
|---|---|---|---|---|---|---|---|
| $V_a$ (V) | $I$ (mA) | EQE | $P_{opt}$ (mW) | $V_a$ (V) | $I$ (mA) | EQE | $P_{opt}$ (mW) |
| 3.50 | 90 | 0.68 | 142 | 3.30 | 46 | 0.69 | 78 |
| 3.55 | 185 | 0.67 | 286 | 3.35 | 101 | 0.68 | 167 |
| 3.60 | 339 | 0.65 | 512 | 3.43 | 297 | 0.66 | 470 |
| 3.70 | 845 | 0.62 | 1219 | 3.50 | 693 | 0.64 | 1045 |
| 3.75 | 1206 | 0.61 | 1698 | 3.55 | 1082 | 0.62 | 1576 |

400 K

| TFFC | | | | TMJ | | | |
|---|---|---|---|---|---|---|---|
| $V_a$ (V) | $I$ (mA) | EQE | $P_{opt}$ (mW) | $V_a$ (V) | $I$ (mA) | EQE | $P_{opt}$ (mW) |
| 3.30 | 64 | 0.67 | 100 | 3.20 | 68 | 0.67 | 110 |
| 3.45 | 429 | 0.64 | 637 | 3.30 | 280 | 0.65 | 432 |
| 3.50 | 672 | 0.63 | 978 | 3.37 | 608 | 0.63 | 904 |
| 3.55 | 987 | 0.61 | 1406 | 3.40 | 802 | 0.62 | 1174 |
| 3.60 | 1387 | 0.60 | 1931 | 3.45 | 1203 | 0.60 | 1710 |

The models used in this work are still in need of many improvements. The QWs with strong polarization fields should be modeled with more accurate quantum-mechanical models. The drift-diffusion model is based on the Boltzmann approximation, which restricts its applicability at high excitation levels. In addition, perfect thermalization of carriers into the lattice temperature is assumed throughout the structures, and this assumption is not strictly valid at the interfaces of abrupt heterostructures. The ohmic contacts are also assumed to be ideal, i.e. with no power losses at the contacts. The low acceptor activation is not modeled in the simulations, and instead all the acceptors are assumed to be ionized.

Possibly the most important idealization, however, is the assumption of ideal extraction of light when calculating the output powers. In reality, a low extraction efficiency may have a profound effect on the overall efficiency. More accurate models for the light propagation in the LED structures are needed to estimate the extraction

efficiency. In addition, in this work the effect of the element mesh is not fully investigated. Using a denser mesh requires more computational resources but is expected to reduce the numerical error of the FEM solutions.

Another way of improving the model would be including the heat equation with the nonradiative recombination processes and resistive losses as source terms. This would also allow simulating the device temperature distribution with different current density values and the connection between the current density and the overall efficiency. The effects of the nonradiative surface recombination are also left out from the models, and they should especially be added at the etched surface of the TMJ LED to give a more realistic picture.

# 8 Conclusions

Basic semiconductor physics was reviewed in this thesis with a focus on the optoelectronic properties of nitride semiconductors and LEDs. The presented material properties, Maxwell's equations, semiconductor transport equations and recombination models were used to construct a numerical 2-dimensional partial differential equation model for LEDs with active regions emitting at two different wavelengths. This was done to study their performance and feasibility for direct efficient white light generation without the use of phosphors. In addition, use of the finite element method in solving the constructed model was briefly reviewed.

The numerical simulations were mainly performed on two different LED geometries, the commercially available thin-film flip-chip (TFFC) LED and a recently proposed transverse multi-quantum well junction (TMJ) LED. The numerical models were solved using *Comsol Multiphysics*. In the modeling, particular interest was paid on calculating the attainable optical powers and corresponding overall efficiencies of the LED structures as well as the effects of the strong internal polarization fields observed in nitride semiconductors. In addition, the effects of the resistive losses in the current spreading layers were studied.

In the numerical results the TMJ LED had a smaller threshold voltage. Also the overall efficiency of the simulated TMJ LED was found to be slightly higher than that of the TFFC LED, mainly due to a smaller resistive power loss. Regarding the injection efficiency and internal quantum efficiency the devices were found to act almost equivalently. It was also found that the spontaneous and piezoelectric polarizations of group III nitrides had a tremendous effect on the materials' operation in LEDs. They effectively created strong electric fields in the QWs and notably reduced the internal quantum efficiencies.

The effects of the resistive potential losses on the spatial distribution of the radiative recombination were studied with different current spreading layer widths, and it was found that these losses fundamentally restrict the usable current values and the LED surface areas. According to the numerical results, reducing the current spreading layer width allows using a higher drive current so that the emission still is spatially homogeneously distributed.

Based on the numerical results, producing white light directly with the simulated structures consisting of only two emitting QWs seems possible. The emission of the simulated structures tends to be more powerful from one of the QWs rather than from both of them at technologically useful current density values, but tailoring of the LED structures is expected to allow tuning the color balance of the produced light. With the information on the current spreading properties of these structures provided by the results of this thesis, it is straightforward to use the presented models for studying structures with more complex active MQW regions in the future works.

Although the commercial GaN-based solid-state lighting devices already show good power efficiency values, their full potential still remains to be reached. Due to the large variation of the band gap in nitride semiconductors, production of high-quality white light is in principle possible without the use of phosphors by only using nitride compositions on a same chip. However, this calls for more theoretical and

computational research conducted on nitride semiconductors as well as new ideas for utilizing the particular properties related to them. For example, the effects of the spontaneous and piezoelectric polarization must be studied further to design structures which minimize their disadvantages or even make use of them somehow.

Furthermore, the simulation results show that the direct current injection in the QWs enabled by the TMJ structure leads to an improved overall efficiency. While it is difficult to give general predictions on the optimal LED structure based on the results presented here, it is safe to say that geometry can have a profound effect on the performance of the LED structure. This indicates that new insights into the effects of LED geometries may also allow further improvements in the performance of LEDs.

# References


[1] *European Commission: Climate Action - More energy efficient.* Cited 10th August 2010. Available at `http://ec.europa.eu/climateaction/eu_action/energy_efficient/index_en.htm`

[2] Navigant Consulting Inc., Radcliffe Advisors Inc. and SSLS Inc. *Multi-Year Program Plan FY'09-FY'15: Solid-State Lighting Research and Development.* Announced in March 2009.

[3] E. F. Schubert and J. K. Kim. Solid-State Light Sources Getting Smart. *Science*, 308, 2005.

[4] J. M. Phillips *et al.* Research challenges to ultra-efficient inorganic solid-state lighting. *Laser & Photonics Reviews*, 1, 2007.

[5] C. de Falco, E. Gatti, A. L. Lacaita and R. Sacco. Quantum-corrected drift-diffusion models for transport in semiconductor devices. *Journal of Computational Physics*, 204, 2005.

[6] J. Singh. *Physics of Semiconductors and Their Heterostructures.* McGraw-Hill, Inc., 1993. ISBN 0-07-057607-6.

[7] J. Sinkkonen. *Puolijohdeteknologian perusteet.* Helsinki University of Technology, 1996. ISBN 951-22-3242-1.

[8] *NSM Archive - Physical Properties of Semiconductors.* Cited 8th June 2010. Available at `http://www.ioffe.ru/SVA/NSM/Semicond/index.html`

[9] J. Tulkki. Fermijakauma puolijohteissa. *Course handout, S-114.1327 Physics III.* Helsinki University of Technology, 2007.

[10] O. Heikkilä. Numerical Modeling of High Efficiency LEDs. *Master's Thesis.* Helsinki University of Technology, 2008.

[11] M. E. Levinshtein, S. L. Rmuyantsev and M. S. Shur. *Properties of Advanced Semiconductor Materials.* John Wiley & Sons, 2001. ISBN 0-471-35827-4.

[12] S. L. Chuang. *Physics of Photonic Devices.* John Wiley & Sons, 2009. ISBN 978-0-470-29319-5.

[13] P. Bhattacharya. *Semiconductor Optoelectronic Devices.* Prentice Hall, 1997. ISBN 0-13-495656-7.

[14] A. Dmitriev and A. Oruzheinikov. The rate of radiative recombination in the nitride semiconductors and alloys. *Journal of Applied Physics*, 86, 1999.

[15] W. Shockley and W. T. Read Jr. Statistics of the Recombinations of Holes and Electrons. *Physical Review*, 87, 1952.

[16] R. Aleksiejunas *et al.* Determination of free carrier bipolar diffusion coefficient and surface recombination velocity of undoped GaN epilayers. *Applied Physics Letters*, 83, 2003.

[17] Y. C. Shen *et al.* Auger recombination in InGaN measured by photoluminescence. *Applied Physics Letters*, 91, 2007.

[18] O. Heikkilä, J. Oksanen and J. Tulkki. Ultimate limit and temperature dependency of light-emitting diode efficiency. *Journal of Applied Physics*, 105, 2009.

[19] W. B Joyce and S. H. Wemple. Steady-State Junction-Current Distributions in Thin Resistive Films on Semiconductor Junctions (Solutions of $\nabla^2 v = \pm e^v$). *Journal of Applied Physics*, 41, 1970.

[20] J. Singh. *Semiconductor Devices: An Introduction.* McGraw-Hill, Inc., 1994. ISBN 0-07-057625-4.

[21] S. Y. Karpov. Visible Light-Emitting Diodes. *Nitride Semiconductor Devices, ed. Joachim Piprek.* Wiley-VCH, 2007. ISBN 978-3-527-40667-8.

[22] D. Delbeke *et al.* High-Efficiency Semiconductor Resonant-Cavity Light-Emitting Diodes: A Review. *IEEE Journal on Selected Topics in Quantum Electronics*, 8, 2002.

[23] O. Heikkilä, J. Oksanen and J. Tulkki. The challenge of unity wall plug efficiency: The effects of internal heating on the efficiency of light-emitting diodes. *Journal of Applied Physics*, 107, 2010.

[24] J. Oksanen and J. Tulkki. Thermophotonic heat pump - a theoretical model and numerical simulations. *Journal of Applied Physics*, 107, 2010.

[25] Th. Gessmann and E. F. Schubert. High-efficiency AlGaInP light-emitting diodes for solid-state lighting applications. *Journal of Applied Physics*, 95, 2004.

[26] S. Reineke *et al.* White organic light-emitting diodes with fluorescent tube efficiency. *Nature*, 459, 2009.

[27] R. Capelli *et al.* Organic light-emitting transistors with an efficiency that outperforms the equivalent light-emitting diodes. *Nature Materials*, 9, 2010.

[28] *Wikimedia Commons.* Cited 20th June 2010. Available at `http://commons.wikimedia.org/wiki/File:CIE1931xy_blank.svg`

[29] H. Amano, N. Sawaki, I. Akasaki and Y. Toyoda. Metalorganic vapor phase epitaxial growth of a high quality GaN film using an AlN buffer layer. *Applied Physics Letters*, 48, 1986.

[30] S. Nakamura, T. Mukai, M. Senoh. Candela-class high-brightness InGaN/AlGaN double-heterostructure blue-light-emitting diodes. *Applied Physics Letters*, 64, 1994.

[31] S. Nakamura *et al.* Room-temperature Continuous-wave operation of InGaN multi-quantum-well structure laser diodes. *Applied Physics Letters*, 69, 1996

[32] J. Piprek. Introduction, *Nitride Semiconductor Devices, ed. Joachim Piprek*. Wiley-VCH, 2007. ISBN 978-3-527-40667-8.

[33] E. F. Schubert. *Light-Emitting Diodes*. Oxford University Press. 2006. ISBN 978-0-521-86538-8.

[34] H. Amano, M. Kito, K. Hiramatsu and I. Akasaki. P-type conduction in Mg-Doped GaN treated with Low-Energy Electron Beam Irradiation (LEEBI). *Japanese Journal of Applied Physics*, 28, 1989.

[35] S. Nakamura, T. Mukai, M. Senoh and N. Iwasa. Thermal Annealing Effects on P-Type Mg-Doped GaN Films. *Japanese Journal of Applied Physics*, 31, 1992.

[36] I. D. Goepfert, E. F. Schubert, A. Osinsky, P. E. Norris and N. N. Faleev. Experimental and theoretical study of acceptor activation and transport properties in p-type $Al_xGa_{1-x}N$/GaN superlattices. *Journal of Applied Physics*, 88, 2000.

[37] J. Simon, V. Protasenko, C. Lian, H. Xing and D. Jena. Polarization-Induced Hole Doping in Wide-Band-Gap Uniaxial Semiconductor Heterostructures. *Science*, 327, 2010.

[38] Y. Xin *et al.* Direct observation of the core structures of threading dislocations in GaN. *Applied Physics Letters*, 72, 1998.

[39] S. Nakamura. The Roles of Structural Imperfections in InGaN-Based Blue Light-Emitting Diodes and Laser Diodes. *Science*, 281, 1998.

[40] F. Bernardini. Spontaneous and Piezoelectric Polarization: Basic Theory vs. Practical Recipes. *Nitride Semiconductor Devices, ed. Joachim Piprek*. Wiley-VCH, 2007. ISBN 978-3-527-40667-8.

[41] M. Levinshtein, S. Rumyantsev and M. Shur. *Handbook Series on Semiconductor Parameters. Volume 2, Ternary and Quaternary III-V Compounds*. World Scientific, 1999. ISBN 981-02-2935-6.

[42] *Wikimedia Commons*. Cited 27th May 2010. Available at `http://commons.wikimedia.org/wiki/File:Wurtzite-kassebaum.gif`

[43] A. Zoroddu, F. Bernardini, P. Ruggerone and V. Fiorentini. First-principles prediction of structure, energetics, formation enthalpy, elastic constants, polarization, and piezoelectric constants of AlN, GaN, and InN: Comparison of local and gradient-corrected density-functional theory. *Physical Review B*, 64, 2001.

[44] V. Fiorentini, F. Bernardini and O. Ambacher. Evidence for nonlinear macroscopic polarizationin III-V nitride alloy heterostructures. *Applied Physics Letters*, 80, 2002.

[45] O. Ambacher *et al.* Role of Spontaneous and Piezoelectric Polarization Induced Effects in Group-III Nitride Based Heterostructures and Devices. *Physica Status Solidi (b)*, 216. Wiley-VCH, 1999.

[46] F. Bernardini and V. Fiorentini. Spontaneous polarization and piezoelectric constants of III-V nitrides. *Physical Review B*, 56, 1997.

[47] S. Suihkonen. Fabrication of InGaN quantum wells for LED applications. *Doctoral Dissertation*. Helsinki University of Technology, 2008.

[48] "Philips Lumileds Thin Film Flip Chip technology delivers the highest performance LEDs for lighting applications." *Press Information, Philips Lumileds*, 2007.

[49] O. B. Shchekin *et al.* High performance thin-film flip-chip InGaN-GaN light-emitting diodes. *Applied Physics Letters*, 89, 2006.

[50] O. Shchekin and D. Sun. Evolutionary new chip design targets lighting systems. *Compound Semiconductor*, 13, 2007.

[51] "Luxeon Rebel Power LED Selected as an EDN Hot 100 Product." *Press Information, Philips Lumileds*, 2010.

[52] G. Chen *et al.* Performance of high-power III-nitride light emitting diodes. *Physica Status Solidi (a)*, 205, 2008.

[53] S.-H. Guol *et al.* Transverse-junction superluminescent diodes at $1.1\,\mu m$ wavelength regime. *Optics Express*, 16, 2008.

[54] S.-H. Guol, M. Z. Zhou, H. W. Huang and J.-W. Shi. Application of transverse junction structure in white-light generation devices: light-emitting diodes and superluminescent diodes. Presentation, *SPIE Photonics West* Conference, San Francisco, 2010.

[55] T. Fujii *et al.* Increase in the extraction efficiency of GaN-based light-emitting diodes via surface roughening. *Applied Physics Letters*, 84, 2004.

[56] M. Lyly and T. Lassila. *Course handout, Mat-1.3650 Finite element method I.* Aalto University, 2010.

[57] Z. Chen. *Finite Element Methods and Their Applications*. Springer, 2005. ISBN 3-540-24078-0.